Defects in lipid homeostasis reflect the function of TANGO2 in phospholipid and neutral lipid metabolism

Agustin Lujan[1], Ombretta Foresti[1], Conor Sugden[1], Nathalie Brouwers[1], Alex Mateo Farre[1], Alessio Vignoli[1], Mahshid Azamian[2], Alicia Turner[3], Jose Wojnacki[1], and Vivek Malhotra[1,4,5]

[1] Centre for Genomic Regulation (CRG), The Barcelona Institute for Science and Technology, Dr. Aiguader 88, 08003 Barcelona, Spain.

[2] Center for Cell and Gene Therapy, Baylor College of Medicine, Houston, TX 77030, USA.

[3] Department of Molecular and Human Genetics, Baylor College of Medicine, Houston, TX 77030, USA.

[4] Universitat Pompeu Fabra (UPF), Barcelona 08002, Spain.

[5] ICREA, Barcelona 08010, Spain.

Corresponding author: Vivek Malhotra

Email: vivek.malhotra@crg.eu

Tel: 34-933160235

Abstract

We show that TANGO2 in mammalian cells localizes predominantly to mitochondria and partially at mitochondria sites juxtaposed to lipid droplets (LDs) and the endoplasmic reticulum. HepG2 cells and fibroblasts of patients lacking TANGO2 exhibit enlarged LDs. Quantitative lipidomics revealed a marked increase in lysophosphatidic acid (LPA) and a concomitant decrease in its biosynthetic precursor phosphatidic acid (PA). These changes were exacerbated in nutrient-starved cells. Based on our data, we suggest that TANGO2 function is linked to acyl-CoA metabolism, which is necessary for the acylation of LPA to generate PA. The defect in acyl-CoA availability impacts the metabolism of many other fatty acids, generates high levels of reactive oxygen (ROS), and promotes lipid peroxidation. We suggest that the increased size of LDs is a combination of enrichment in peroxidized lipids and a defect in their catabolism. Our findings help explain the physiological consequence of mutations in TANGO2 that induce acute metabolic crises, including rhabdomyolysis, cardiomyopathy, and cardiac arrhythmias, often leading to fatality upon starvation and stress.

Introduction

In 2006, we reported a collection of new genes required for transport and organization of the Golgi complex in drosophila (Bard et al., 2006). These genes, monikered TANGO, include TANGO1, a transmembrane protein required for the organization of endoplasmic reticulum (ER) exit sites where it collects bulky molecules like collagens and stabilizes transient inter-organelle tunnels for their export to the next compartment of the secretory pathway (Raote and Malhotra, 2021).

TANGO2, a gene unrelated to TANGO1, lacks a transmembrane domain and is reported to be cytosolic and also localized to mitochondria (Jennions et al., 2019; Milev et al., 2021). TANGO2 affects ER to Golgi transport and mitochondria physiology; however, its precise role in these compartments is unknown (Bérat et al., 2021; Milev et al., 2021; Mingirulli et al., 2020). Mutations in TANGO2 result in metabolic encephalopathy and arrhythmias and these conditions are exacerbated upon nutrient starvation, often leading to fatality (Kremer et al., 2016; Lalani et al., 2016). What is the physiological role of TANGO2, and how do mutations in TANGO2 lead to fatality in conditions of starvation?

We show here that TANGO2 in mammalian cells localizes predominantly to mitochondria, but also partially to sites where the ER and lipid droplets

(LDs) are juxtaposed to mitochondria. Knockdown of TANGO2 increased the size of LDs and elevated intracellular reactive oxygen species (ROS) levels. Mass spectrometric quantification of cellular lipids revealed that TANGO2-deficient cells exhibited markedly high lysophosphatidic acid (LPA) and low levels of phosphatidic acid (PA). These cells were also highly reduced in cardiolipin (CL), which is ordinarily produced from PA. Moreover, changes in these cellular properties were further exacerbated in cells cultured in low-nutrient media. Many of these features match properties of cells derived from patients with mutations in TANGO2. Based on our data, we propose that TANGO2 functions in lipid homeostasis at the level of acyl-CoA metabolism, and defects in lipid metabolism are the main cause of starvation-induced acute rhabdomyolysis, cardiomyopathy, and cardiac arrhythmias.

Results

TANGO2 localizes predominantly to the mitochondria and transiently to LDs and ER

In humans, six isoforms of TANGO2 are produced by alternative splicing. The TANGO2-1 (TNG2_HUMAN·Q6ICL3-1) and TANGO2-2 (TNG2_HUMAN·Q6ICL3-2) isoforms are most similar to their orthologs, such as hrg-9 in worms, ygr127w in yeast, and tango2 in zebrafish (Figure 1 A-B). It is important to note that the anti-Tango2 antibody we have used here recognizes both isoforms in human cells, and tagged versions of both isoforms show the same intracellular location (Figure 1 A). As shown in the following sections, siRNA-based depletion affects all isoforms. Therefore, the effect of TANGO2 depletion on cell physiology is a result of reduction in the levels of all isoforms.

A

B

	TCS	Identity	Coverage
TANGO2.isoform1	49	31%	89%
TANGO2.isoform2	49	33%	80%
TANGO2.isoform3	48	30%	87%
TANGO2.isoform4	48	30%	84%
TANGO2.isoform5	46	28%	76%
TANGO2.isoform6	48	30%	70%

Figure 1. TANGO2 orthologs. A) In silico sequence alignment of TANGO2 orthologs in human (*H. sapiens*), zebrafish (*D. rerio*), fruit fly (*D. melanogaster*), worm (*C. elegans*), and yeast (*S. cerevisiae*) using T-COFFEE software. The transitive consistency score (TCS) color code indicates the agreement between the library and the considered alignment. The TCS scale goes from blue (less consistent) to dark pink (high reliability and more accurate agreement) brick regions. The color line (cons) below the alignment indicates the consensus score of every column. Residue numbering is based on the full-length of the human TANGO2 protein (TNG2_HUMAN·Q6ICL3). **B)** Multiple sequence alignment (MSA) of each human TANGO2 isoform with species orthologs. The TCS identifies the most correct alignment positions in MSA, the Identity evaluates the sequence function, and the Coverage describes the average number of reads that align to known reference bases.

Previous published data showed conflicting results on the intracellular location of TANGO2 (Heiman et al., 2022; Jennions et al., 2019; Milev et al., 2021). Unfortunately, the commercial anti-TANGO2 antibodies are not suitable for immunofluorescence analysis. Therefore, we monitored the location of TANGO2 distribution dynamically in living cells. We generated C-terminally tagged version of Tango2 by in frame fusion with either mScarlet (TANGO2.Iso1-mScarlet) or EGFP (TANGO2.Iso1-EGFP). By transient transfections in HepG2 cells, we co-expressed these forms of TANGO2 with fluorescent markers of various subcellular organelles including, mitochondria (Mito-mTurquoise), ER (ER-mTurquoise), peroxisomes (Peroxisome-mTurquoise), and LDs (GPAT4-mNeonGreen). All images were acquired by live-cell confocal time-lapse microscopy to avoid fixation artefacts. We observed high co-localization (Pearson coefficient, r=0.88) between TANGO2 and the mitochondria marker. TANGO2 was also enriched at sites of mitochondria closely juxtaposed to ER and LDs (Figure 2 A). To further ascertain the location of TANGO2, we monitored its intracellular locale with respect to ER and LDs in fixed cells. HepG2 cells were co-transfected with TANGO2-mScarlet and VAPB-NeonGreen - a protein located in the ER membrane and in the mitochondria-associated membrane (MAM) sites (Figure 2 - Figure supplement 1 A), or with the LD marker GPAT4-NeonGreen (Figure 2 - Figure supplement 1 B). We observed TANGO2-Scarlet and the specific

markers of ER and LDs in close position in XY, XZ and YZ planes (Figure 2 - Figure supplement 1 A-B).

To confirm the topology of TANGO2-mScarlet in the mitochondria membrane, we evaluated the proximity between TANGO2 and Tom20 - a protein marker of the outer mitochondria membrane (OMM) - by Förster resonance energy transfer (FRET) microscopy in fixed cells. This procedure analyzes the radiation energy transfer from an excited fluorescent molecule (called the donor) to an acceptor molecule; this occurs when both molecules are within a range of 1 to 10 nm from each other (Broussard et al., 2013). To explore the proximity of TANGO2 to Tom20 , HepG2 cells were transfected with TANGO2.mScarlet (red), fixed, and stained with anti-Tom20 antibody (green) followed by Alexa 633 secondary antibody. After photobleaching (white square) of Alexa 633 we observed a significant increase in mScarlet-fluorescence intensity compared to an unbleached region (p=0.0002), confirming a FRET signal (Figure 2 B-D).

To avoid potential artefacts from an uneven or abnormal protein expression by transient transfection, we generated stable cell lines expressing low levels of the C-terminally EGFP-tagged TANGO2 using lentiviral infection (Tandon et al., 2018). Live imaging of stable cell lines revealed that TANGO2-GFP localizes predominantly to mitochondria (Figure 2 - Figure supplement 1 C). We also observed a diffuse cytosolic staining (Figure 2 -

Figure supplement 1 D). To check whether TANGO2-EGFP is cleaved in our experimental conditions giving rise to different forms, we verified the size of expressed construct by SDS/PAGE followed by western blotting with anti-GFP antibody (Figure 2 - Figure supplement 1 E). This revealed a single band that matches the expected molecular weight of EGFP-tagged TANGO2.

It is therefore reasonable to conclude that despite lacking a transmembrane-domain, TANGO2 is attached predominantly to the mitochondria outer membrane and at mitochondria sites that are juxtaposed to the ER and the LDs. TANGO2 likely cycles between the cytoplasm and the membrane.

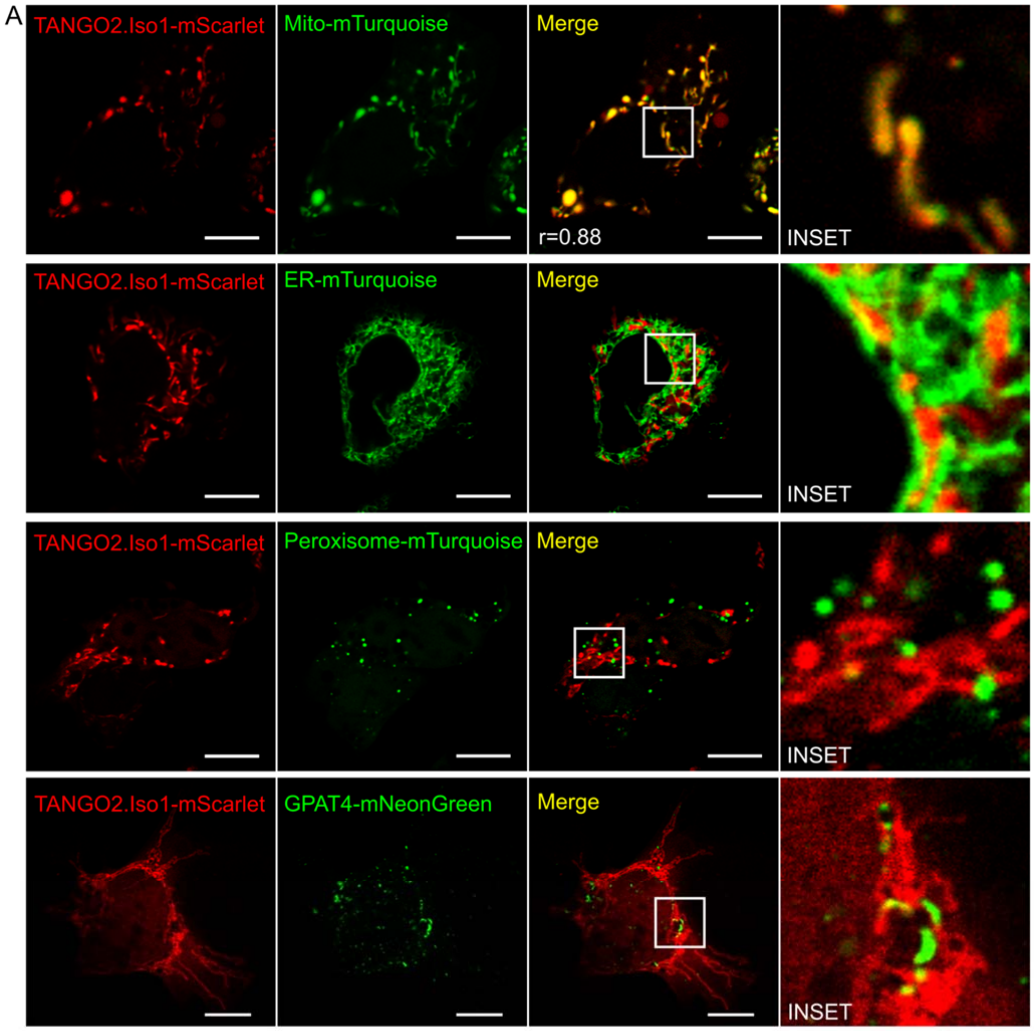
A
TANGO2.Iso1-mScarlet
Mito-mTurquoise
Merge
r=0.88
INSET
TANGO2.Iso1-mScarlet
ER-mTurquoise
Merge
INSET
TANGO2.Iso1-mScarlet
Peroxisome-mTurquoise
Merge
INSET
TANGO2.Iso1-mScarlet
GPAT4-mNeonGreen
Merge
INSET

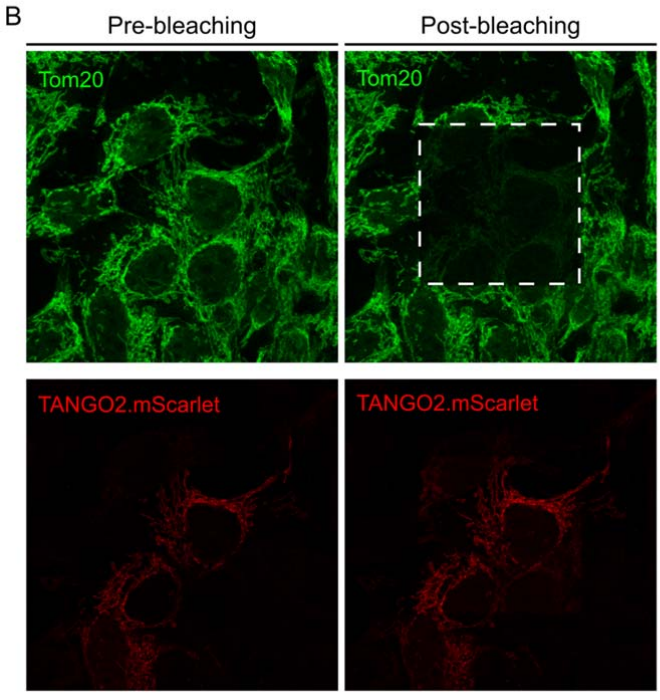
B
Pre-bleaching
Post-bleaching
Tom20
Tom20
TANGO2.mScarlet
TANGO2.mScarlet

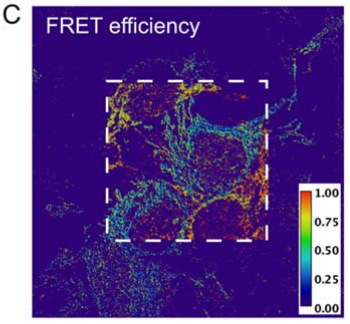
C
FRET efficiency
1.00
0.75
0.50
0.25
0.00

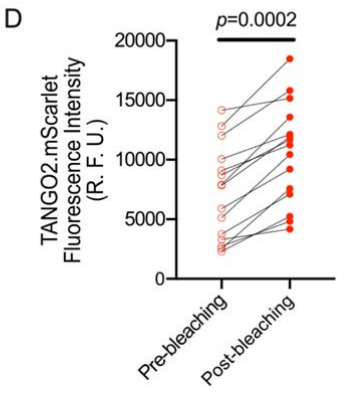
D
p=0.0002
TANGO2.mScarlet
Fluorescence Intensity
(R. F. U.)
20000
15000
10000
5000
0
Pre-bleaching
Post-bleaching

Figure 2. TANGO2 location in HepG2 cells. A) Cells expressing TANGO2.Iso1-mScarlet co-transfected with Mitochondria-pmTurquoise2 (Mito-mTurquoise), ER-pmTurquoise2 (ER-mTurquoise), Peroxisome-SKL-mTurquoise2 (Peroxisome-mTurquoise) or GPAT4-hairpin-mNeonGreen (GPAT4-mNeonGreen) to detect lipid droplets. The yellow color indicates colocalization between both red and green labels. Pearson coefficient (r) was calculated with the coloc2 plugin in ImageJ software. Images are representative of three independent experiments. Scale bars = 10 μm. **B-D)** HeLa cells were transfected with TANGO2.mScarlet, fixed, and incubated with anti-Tom20 followed by Alexa-633 secondary antibodies. **B)** Representative image of the fluorescence intensity in the acceptor (upper panels) and donor (bottom panels) channels before (left panels) and after photobleaching (right panels) of the acceptor. **C)** Representative map of FRET efficiency calculated from the donor fluorescence intensity as described in the materials and methods section. **D)** Quantification of the increase in fluorescence intensity of the donor channel (TANGO2.mScarlet) after photobleaching (n = 15 cells). R. F. U., means relative fluorescence units.

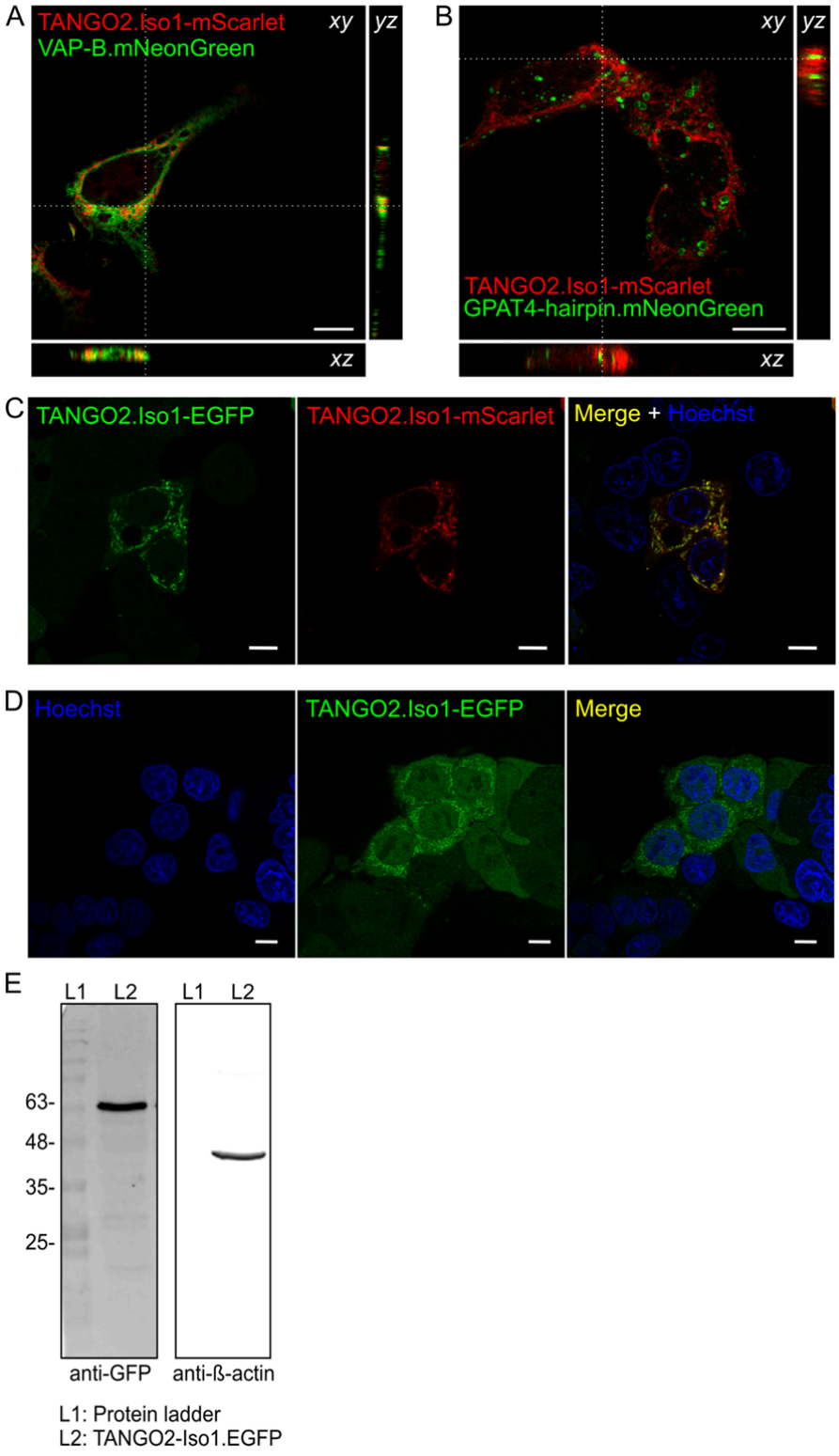

177

178 **Figure 2 - Figure supplement 1. Intact expressed tagged-TANGO2 is in close**

179 **proximity to ER and LDs. A)** HepG2 cells expressing TANGO2.Iso1-mScarlet and

180 co-transfected with VAP-B.mNeonGreen to detect ER membranes. The dotted line in

the XY plane shows the slice projected in the ZY and XZ axes. The yellow color indicates colocalization between red and green labels in the different projections. Scale bars = 10 µm. **B)** HepG2 cells expressing TANGO2.Iso1-mScarlet and co-transfected with GPAT4-hairpin.mNeonGreen to detect LDs. The dotted line in the XY plane shows the slice projected in the ZY and XZ axes. The yellow color indicates colocalization between red and green labels in the different projections. Scale bars = 10 µm. **C)** TANGO2.Iso1-EGFP HepG2 stable cells were transiently transfected with TANGO2.Iso1-mScarlet (red), and labeled with Hoechst (blue). Merge shows all overlapping channels. **D)** TANGO2.Iso1-EGFP (green) HepG2 stable cell was labeled with Hoechst (blue). **E)** Immunoblot analysis of TANGO2.Iso1-EGFP HepG2 stable cell line incubated with anti-GFP and anti-ß-actin. Anti-ß-actin was used as a loading control.

TANGO2 lacking cells contain larger Lipid droplets (LDs)

As shown above, TANGO2 frequently appears at sites that are marked by LDs. This prompted us to test whether cells lacking TANGO2 are affected in any aspect of LDs. We silenced TANGO2 (siTANGO2) by standard siRNA based methods. A control was generated with non-targeting siRNA and described henceforth as Mock. The silencing procedure reduced TANGO2 levels by ~45% after one round of siRNA transfection. However, after two sequential rounds of transfection, a ~75% reduction in TANGO2 levels was evident (Figure 3 - Figure supplement 1 A). We have used double sequential transfections to reduce TANGO2 levels in all

204 experiments that follow (Figure 3 - Figure supplement 1 B). Mock HepG2
205 cells and TANGO2-depleted cells were cultured in medium (DMEM)
206 supplemented with 10% Fetal Bovine Serum (FBS) (DMEM complete) or
207 OptiMEM without FBS (starvation) for 4 h. Cells were then incubated with
208 membrane permeant neutral lipid marker HCS LipidTOX™ Deep Red
209 (red) and the DNA marker Hoechst-33342 (blue) for 30 min at 37 ºC
210 followed by live-cell imaging. LDs were consistently larger in TANGO2-
211 depleted cells compared to mock cells (Figure 3 A, left panel). Moreover,
212 nutrient deprived TANGO2-depleted cells (Starvation; Figure 3 A, right
213 panel) had even larger LDs. To confirm that these structures are indeed
214 LDs, TANGO2-depleted HepG2 cells were fixed and visualized with an
215 antibody to the LD-resident protein ADRP (red). Nuclear DNA in these
216 cells was labeled with DAPI (blue). There was indeed an increase in the
217 size of ADRP-containing LDs upon depletion of TANGO2 (Figure 3 B).
218 We developed a macro for Image J Software, to quantify this increased
219 retention of neutral lipids upon depletion of TANGO2. This procedure
220 analyzes Z-stack images to determine the number and volume of each
221 LipidTOX-positive particle. Five samples were used for each condition,
222 with a total of 67 Mock cells and 75 TANGO2-depleted cells, respectively.
223 As shown in Figure 3, total volume of LDs per cell (panel C) and the
224 volume of each LD (panel D) was significantly higher in TANGO2-
225 depleted compared to the Mock cells (p=0.0005 and p=0.002, respectively).

However, the number of LDs in each cell remain the same regardless of the TANGO2 levels (Figure 3 E). Therefore, the increase in size is not caused by fusion of smaller LDs under these experimental conditions. To further analyze the effect of TANGO2 on LDs size, we added 120 nM Oleic acid (OA), which is known to potentiate LD formation, at 37 º C for 6 h to TANGO2 transiently depleted HepG2 cells (Mock vs. siTANGO2) and fibroblasts from TANGO2 deficiency disorder (TDD)-donors (WT vs. TAN043. Changes in the total volume of LDs were evaluated by fluorescence intensity (FI) of allophycocyanin (APC) corresponding to HCS LipidTOX with flow cytometry (Figure 3 - Figure supplement 1 C). Three independent experiments were analyzed for each condition in triplicate. The loss of TANGO2 revealed a significant increase in total LDs volume compared to Mock HepG2 cells (Figure 3 F) or wild-type fibroblasts (Figure 3 G). To reveal the cause for increased volume of LDs we analyzed their metabolism. To explore LD biogenesis in WT and TAN043 fibroblast, we generated three independent medium conditions of DMEM complete (control), adding 120 nM OA at 37ºC for 6 h in DMEM complete (+OA), or adding 120 nM OA at 37ºC for 6 h with the lipolysis inhibitor diethylumbelliferyl phosphate (DEUP) in DMEM complete (+OA+DEUP) (Figure 3 - Figure supplement 1 D). The inhibition of lipolysis in complete-medium conditions revealed a greater increase of LipidTOX marker in TANGO2-depleted fibroblasts compared to WT

(Figure 3 H). This result suggests a more prominent activation of the LD biogenesis in TANGO2-lacking fibroblasts. To test the effect on LD consumption, we added 240 nM OA at 37ºC for 12 h in DMEM complete medium. We then changed the supplemented OA medium with fresh-complete medium including DEUP to synchronize lipolysis initiation (+OA+DEUP), nutrient-free medium to activate starvation (+OA+Starvation) or nutrient-free medium with DEUP to block lipolysis (+OA+Starvation+DEUP) (Figure 3 - Figure supplement 1 E). Fasting induction demonstrated a drastic alteration of the lipolytic pathway in TANGO2-depleted fibroblasts compared to WT fibroblasts (Figure 3 I). Altogether, depletion of TANGO2 displays substantial enlargement of LDs by a combination of increased biogenesis and a pronounced defect in lipolysis.

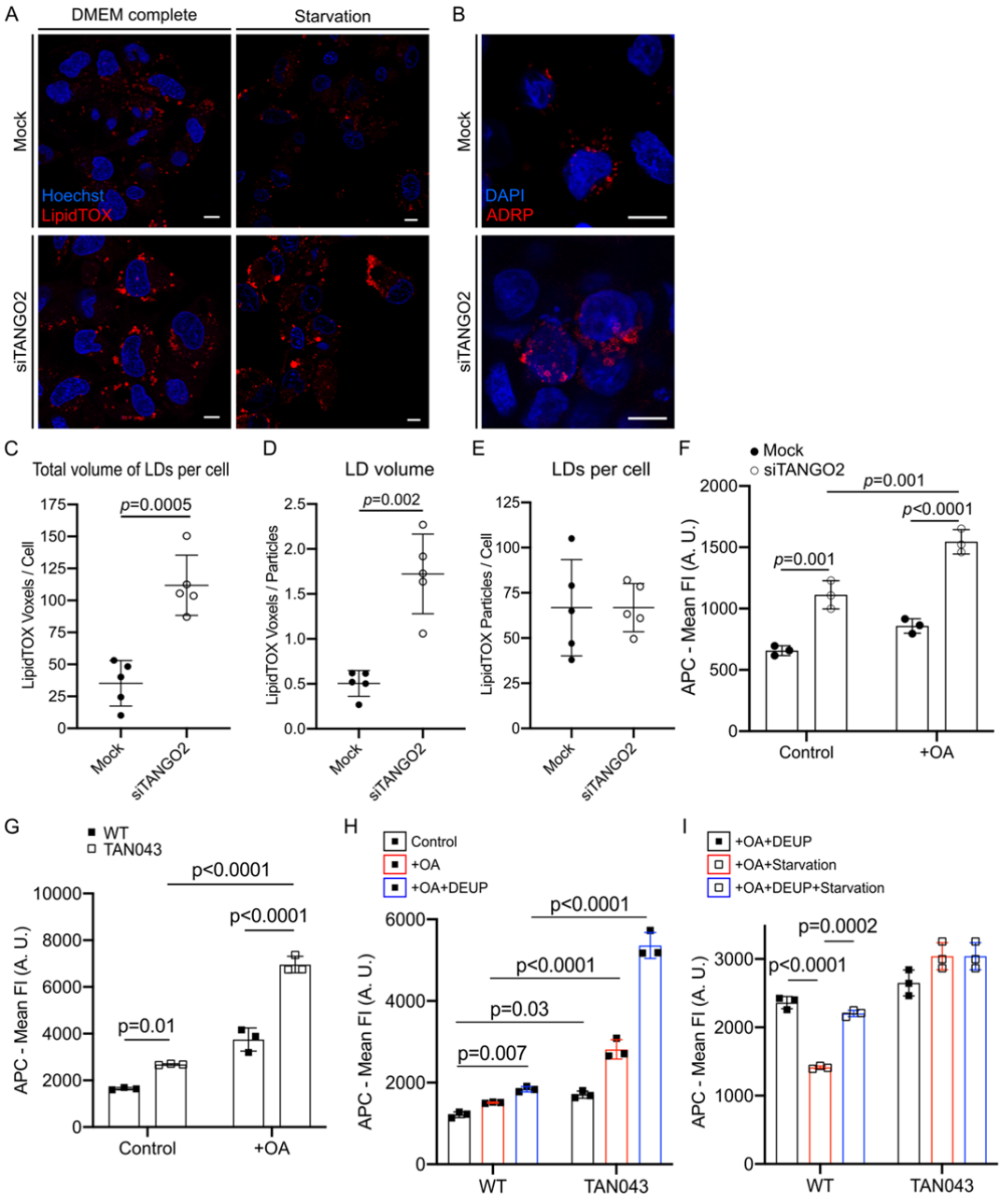

Figure 3. TANGO2 depletion affects LDs' size, biogenesis, and lipolysis. A) Confocal images of HCS LipidTOX Deep Red marker (red) and Hoechst-33342 (blue) in mock (top) and TANGO2-depleted (bottom) HepG2 cells cultured in control conditions (DMEM complete; left panel) or starved of nutrients (starvation; right panel). Scale bars = 10 µm. **B)** Mock (top) and TANGO2-depleted (bottom) cells in control conditions were fixed and incubated with anti-ADRP (red) and DAPI (blue). Scale bars

= 10 µm. C-E) Quantification of LDs in mock (n=67 cells) and TANGO2-depleted (n=75 cells) cells in five samples for each condition by an ImageJ macro developed in our lab (open code access in Materials and Methods). **C)** Total volume of LDs present per cell. **D)** Volume of each LD in a cell. **E)** Number of LDs per cell. **F-G)** Quantification of total LD volume in DMEM complete medium (control) and supplemented with 120nM Oleic acid (+OA) using HCS LipidTOX Deep Red marker by flow cytometry. F) Mean fluorescence intensity (mean FI) of APC detected in Mock and TANGO2-depleted HepG2 cells in three different samples of each condition. **G)** Mean fluorescence intensity (mean FI) of APC detected in wild-type (WT) and TANGO2 deficient disease (TAN043) fibroblasts in three different samples of each condition. **H)** Quantification of total LD's volume in DMEM complete medium (control), supplemented with 120nM Oleic acid (+OA), or supplemented with 120nM OA and 500µM DEUP in WT and TAN043 fibroblasts by flow cytometry. **I)** Quantification of total LD volume after supplementation with 240nM OA for 12 h, washed and starved for 5 h with DEUP in WT and TAN043 fibroblasts by flow cytometry. Images and graphs are representatives of three independent experiments. In graphs, boxes and bars are the mean ± SD., A.U. means arbitrary units.

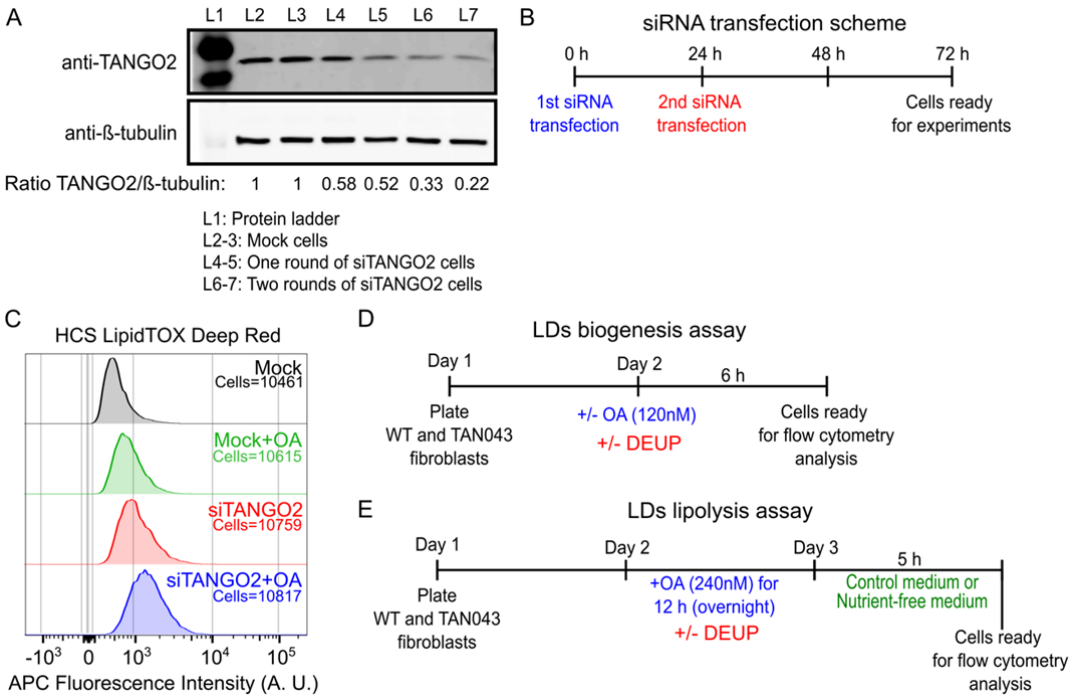

Figure 3 - Figure supplement 1. Depletion of TANGO2 in HepG2 cells. A) Immunoblot analysis of HepG2 wild type (L2-3) cells silenced after one (L4-5) or two (L6-7) rounds of TANGO2 siRNA transfection. **B)** Double siRNA transfection scheme used to reduce endogenous TANGO2 levels. **C)** Mock and TANGO2-depleted HepG2 cells maintained in control conditions or with 120 nM Oleic acid (OA), and incubated with HCS LipidTOX Deep Red for 30 min before flow cytometry analysis. Neutral lipids were detected by measuring the fluorescence intensity of APC. A.U., means arbitrary units. **D)** Scheme of the method used for the neutral lipids biogenesis analysis in WT and TAN043 fibroblasts. **E)** Scheme of the method used for the neutral lipids lipolysis analysis induced by nutrient-fasting in WT and TAN043 fibroblasts.

TANGO2 depletion affects the quantities of specific lipids

A change in the size of LDs in TANGO2-depleted cells prompted us to analyze changes in the cellular lipid composition. Also of note is the

observation that patients with TANGO2 deficiency suffer metabolic crises upon fasting, which suggests impairment in lipid metabolism. Mock cells (Mock), TANGO2-depleted cells (siTANGO2), starved mock cells (Starvation) and starved TANGO2-depleted cells (siTANGO2 starvation) were analyzed in triplicates to quantitate their total lipid composition (Lipotype GmbH). We used the mol percent fraction (molp) analyses because that enables comparisons between the lipidomic profiles of different conditions, disregarding the absolute amount of lipids (Figure 4 - Figure supplement 1 A). However, we also report the absolute levels of lipids in our conditions (Figure 4 - Figure supplement 1 B-C).

First, to monitor the effect of physiological starvation, we compared samples of mock cells under control and starvation conditions (Figure 4, left panel). Upon starvation, lysophosphatidic acid (LPA) levels are reduced, whereas phosphatidylcholine (PC), lysophosphoglycerol (LPG), phosphoglycerol (PG) and phosphatidic acid (PA) levels are notably increased (Figure 4, left panel). LPA is used to produce PA, which is a precursor of PG and mitochondria-specific cardiolipin (CL).

Second, to monitor the effect TANGO2 depletion, we compared samples of Mock and TANGO2-depleted cells grown in normal condition (Figure 4, middle panel). TANGO2-depleted cells show an increase in levels of LPA and reduction in PA and CL levels. There was also an increase in most

lyso-phospholipids and a reduction in the corresponding phospholipids (Figure 4, middle panel).

Last, to monitor the combine effect of starvation and TANGO2 depletion, we compared starved TANGO2-depleted cells with mock starved cells (Figure 4, right panel). Importantly, starving TANGO2-depleted cells exhibited a further increase in LPA and decrease in PA levels (Figure 4, right panel). Moreover, in TANGO2-depleted cells, LPG levels are reduced and there is a dramatic reduction in PG levels. The levels of these two lipids are further reduced in early starvation. We suggest that when PA levels are low, the cells use LPG and PG to produce CL in starving TANGO2-depleted cells and this is the likely reason for the partial restoration of CL levels under these conditions. These data show that nutrient-starved TANGO2-depleted cells have a dramatic change in their LPA to PA ratio and there is a subsequent defect in the homeostasis of additional fatty acids.

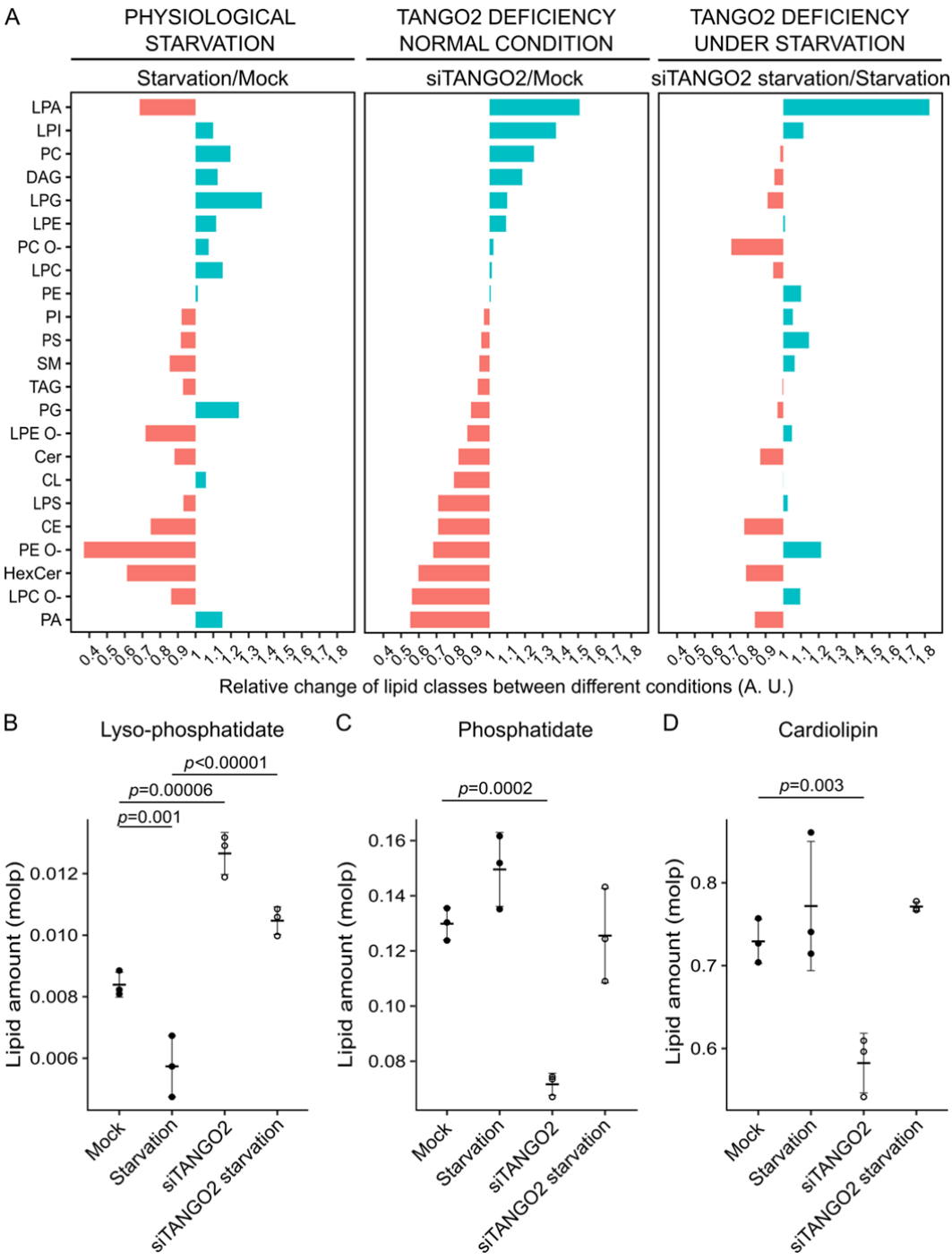

Figure 4. Lipidomics of TANGO2-depleted cells for comparison with control and nutrient-starved cells. A) Relative change of lipid class according to different conditions: physiological starvation (left panel), TANGO2-depleted cells in control conditions (middle panel), and TANGO2-depleted cells upon nutrient starvation (right panel). A.U., means arbitrary units. **B)** Quantification of LPA changes in mock and

TANGO2-depleted cells expressed in mol percent (molp) fractions. **C)** Quantification of PA changes in mock and TANGO2-depleted cells expressed in molp fractions. **D)** Quantification of CL changes in mock and TANGO2-depleted cells expressed in molp fractions. Data is representative of three independent experiments. In graphs, boxes are the mean ± SD.

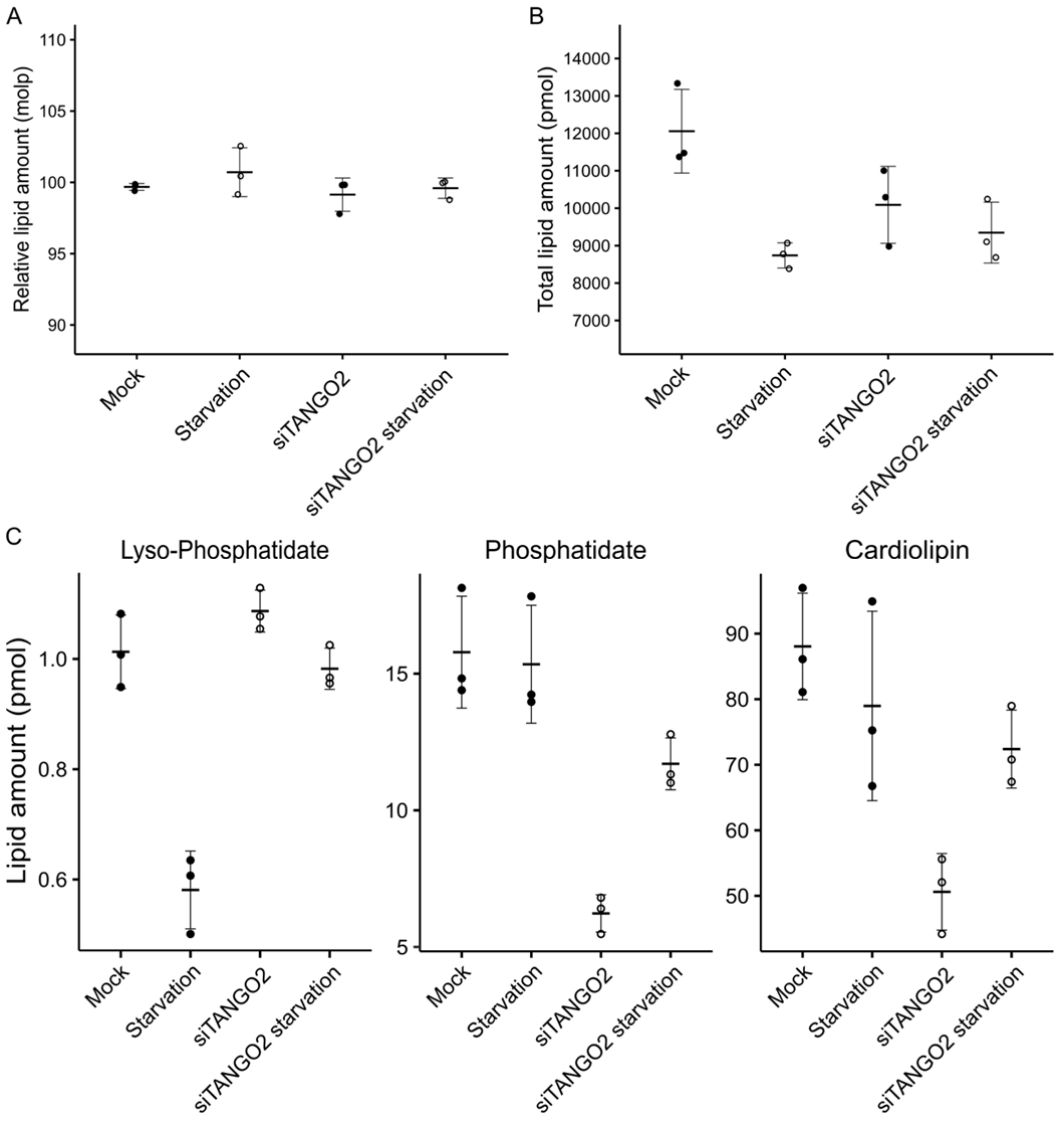

Figure 4 - Figure supplement 1. Absolute values comparison of lipids in HepG2 mock and TANGO2-depleted cells. A) Relative levels of lipids in mock and TANGO2-depleted cells in control and nutrient-starved conditions in mol percent

fraction (molp). **B)** Quantification of the absolute amount of lipids in mock and TANGO2-depleted cells in control and nutrient-starved conditions in pico-mol (pmol). **C)** Quantification of the absolute amount of lyso-phosphatidic acid (LPA) in mock and TANGO2-depleted cells in control and nutrient-starved conditions in pico-mol (pmol). **D)** Quantification of the absolute amount of phosphatidic acid (PA) in mock and TANGO2-depleted cells in control and nutrient-starved conditions in pico-mol (pmol). **E)** Quantification of the absolute amount of cardiolipin (CL) in mock and TANGO2-depleted cells in control and nutrient-starved conditions in pico-mol (pmol).

The loss of TANGO2 affects the levels of enzymes involved in the metabolism of phospholipids and neutral lipids

Changes in the lipid profiles of TANGO2-depleted cells led us to analyze enzymes involved in lipid metabolism. PA has a central role as precursor of all components synthesized in the phospholipid biosynthetic pathway (Gonzalez-Baro and Coleman, 2017). In short, the glycerol-3-phosphate acyltransferases (GPATs) located in the ER (GPAT3/4) and OMM (GPAT1/2) membranes, catalyze the conversion of glycerol-3-phosphate (G3P) to LPA, by transferring a saturated fatty acid from Acyl-CoA. Then, the family of 1-acyl-sn-glycerol-3-phosphate acyltransferases (AGPATs), with lysophosphatidic acid acyltransferase (LPAAT) enzymatic activity, promote addition of an unsaturated fatty acid from Acyl-CoA to LPA to form PA. Once formed, PA can generate diacylglycerol (DAG) after

dephosphorylation by PA phosphatase enzymes (LPINs), or can reconvert to LPA by the action of phospholipase A2 (PLA2) (Lu and Claypool, 2015). The expression of 13 enzymes involved in the phospholipid biosynthetic pathway was measured in three independent experiments by reverse transcription-quantitative polymerase chain reaction (RT-qPCR). RNA extraction was performed in Mock and TANGO2-depleted HepG2 cells in complete medium and starvation medium. For mRNA quantification, we used GAPDH as a reference gene in all conditions. RT-qPCR graphs showed the normalized mRNA expression of each enzyme in TANGO2-depleted cells compared to Mock cells in three independent experiments. These results revealed an increase in GPAT3 and AGPAT1 mRNA expression in TANGO2-depleted cells compared to Mock cells in both control and fasting conditions (Figure 5 A-B). Interestingly, AGPAT3 mRNA expression was decreased in control conditions but significantly increased in a nutrient-free conditioned medium. Furthermore, AGPAT5 mRNA expression was significantly higher in control conditions but not in nutrient deprivation conditions. However, the opposite was seen for AGPAT2 mRNA expression.

The overexpression of AGPAT1 and AGPAT3 enzymes should increase PA production, but TANGO2 deficiency showed a decrease in the PA lipid profile by lipidomic analysis (Figure 4).

Although further enzymatic studies should explore their location and functional activity, these data suggests that decreased production of PA triggers mechanisms to re-establish the physiological levels of this essential component, but lack of TANGO2 prevents this restorative mechanism.

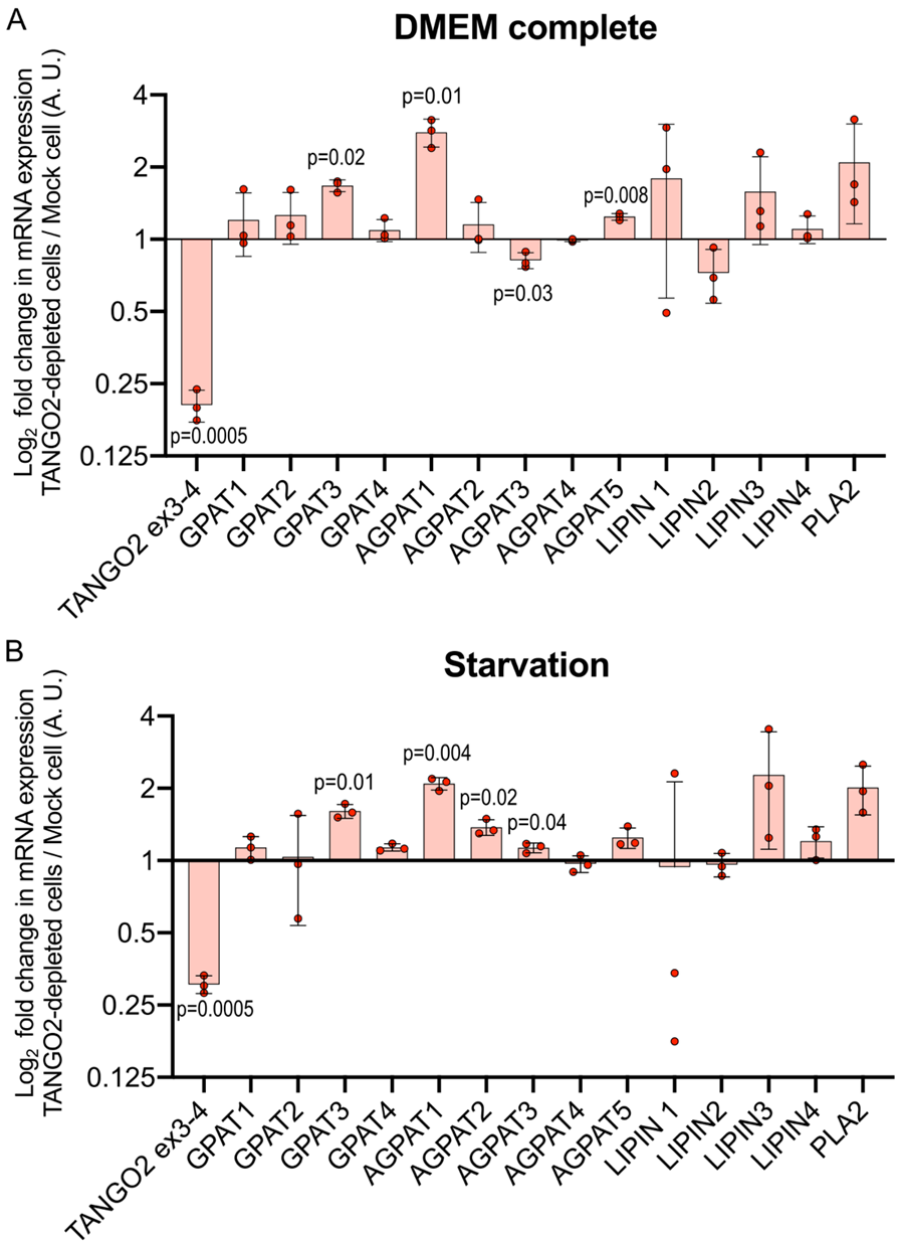

Figure 5. TANGO2 depletion impacts enzymes of lipid metabolism. RT-qPCR analyses of TANGO2-depleted HepG2 cells compared to mock cells in normal **(A)** and

starvation **(B)** conditions. Three biological repeats were performed for each condition. Values were normalized to GAPDH and graphed as log fold change relative to Mock cells of each condition. Statistical significance was determined using a simple unpaired Student's t-test with subsequent Welch's correction analysis between TANGO2-depleted and Mock cells for each enzyme. A.U., means arbitrary units.

TANGO2-depleted cells exhibit increased reactive oxygen species (ROS) and lipid peroxidation

Given that TANGO2 localizes to mitochondria and an earlier report of increased mitochondria-ROS in cells of patients with a TANGO2 deficiency (Heiman et al., 2022), prompted us to test this feature in our experimental conditions. Mitochondria produce ROS at the inner mitochondria membrane during oxidative phosphorylation. ROS produced as a byproduct of ATP synthesis is useful for cells, but high levels of ROS, unless scavenged, are toxic (Bhatti et al., 2017). Mock HepG2 cells (Mock), TANGO2 transiently depleted cells (siTANGO2), wild-type human fibroblasts (WT), and TANGO2 knock-out cells from TDD-patients (TAN043) in complete medium or starvation medium, were incubated for 20 min with CellROX Deep Red reagent to measure cellular ROS levels and MitoTracker Green to measure total mitochondria mass by flow cytometry analysis. Cell viability was measured by using CellTrace Calcein

Green AM. DNA specific DAPI was used to test that TANGO2 silencing did not induce cell death in our samples (Figure 6 - Figure supplement 1). To determine the total mitochondria mass, we analyzed the fluorescence intensity (FI) of fluorescein isothiocyanate (FITC) corresponding to MitoTracker Green for all samples by flow cytometry (Figure 6 A). The statistical analysis shows the mean FI (MFI) of FITC in three independent experiments. The results reveal no significant difference in total mitochondria mass in TANGO2-depleted cells compared to controls (Figure 6 B). To measure ROS production in these experimental conditions, we analyzed differences in FI of APC corresponding to CellROX marker (Figure 6 C). The data show that depletion of TANGO2 significantly increased ROS levels, which are further elevated upon nutrient starvation (Figure 6 D). As we observed a significant difference in the mitochondria mass between fibroblasts from healthy and TDD donors, we analyzed ROS levels by the ratio between CellROX and MitoTracker markers. These results corroborate that TANGO2-lacking fibroblasts have higher ROS levels than WT fibroblasts (Figure 6 E).

Since the increase in ROS damage cellular components such as DNA, proteins, and lipids, we analyzed the peroxidation state of lipids. HepG2 cells transiently depleted of TANGO2 (Mock vs. siTANGO2) and fibroblasts derived from TDD-donors (WT vs. TAN043) were incubated for 30 min with an Image-iT Lipid Peroxidation kit, a sensitive fluorescent

445 reporter for measuring total lipid peroxidation, by flow cytometry. In a
446 reduced state, the maximal emission of the sensor is 591 nm, corresponding
447 to the FI of Phycoerythrin (PE) (Figure 6 F, left panel). Upon oxidation, the
448 reagent shifts the fluorescence emission peak from ~590 nm to ~510 nm
449 corresponding to the FI of FITC (Figure 6 F, right panel). To determine
450 lipid peroxidation, we analyzed the MFI ratio between PE and FITC for all
451 samples (Figure 6 G and H). The statistical analysis shows the fold change
452 of reduced/oxidized lipids in three independent experiments. The results
453 show that rise in ROS production provokes an increase in lipid
454 peroxidation of TANGO2-depleted HepG2 cells (Figure 6 G) and TAN043
455 human fibroblasts (Figure 6 H).
456 Altogether, these data show that TANGO2 depletion causes unsaturated
457 lipid peroxidation, which is known to alter lipid quality.
458

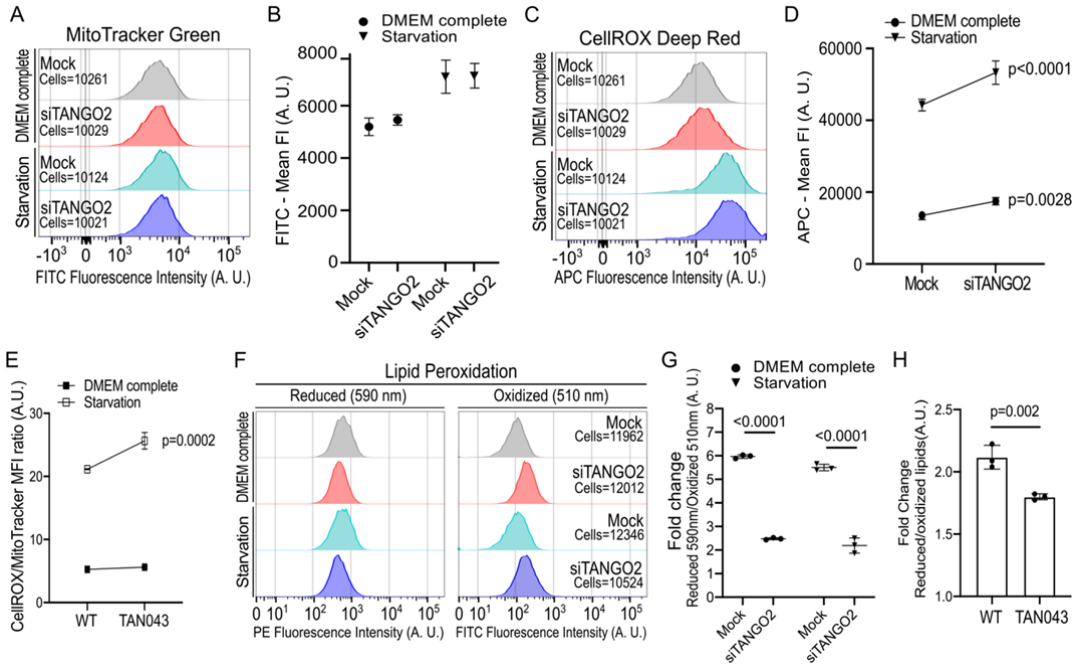

459

460 **Figure 6. TANGO2-depleted cells exhibit increased ROS levels and lipid**
461 **peroxidation. A-D)** Mock and TANGO2-depleted cells were incubated in control
462 conditions (DMEM complete) or in a low nutrient medium (Starvation) for 4 h. Cells
463 were incubated with CellROX Deep Red to detect ROS levels and MitoTracker Green
464 to monitor mitochondria mass. **A)** Mitochondria mass was detected by measuring the
465 fluorescence intensity of FITC by flow cytometry. **B)** The mean fluorescence intensity
466 (Mean FI) of FITC was measured in three different samples of each condition. **C)**
467 Cellular ROS levels were detected by measuring the fluorescence intensity of APC by
468 flow cytometry. **D)** The mean fluorescence intensity of APC was measured in three
469 different samples of each condition. **E)** Ratio between ROS levels (CellROX) and
470 mitochondria mass (MitoTracker) was measured in WT and TAN043 fibroblasts by
471 flow cytometry in three independent experiments. **F)** Lipid peroxidation in HepG2 and
472 fibroblasts was measured by detecting the mean fluorescence intensity change between
473 PE and FITC spectral emissions by flow cytometry. **G)** The fold change shows the ratio
474 between reduced and oxidized lipid species in Mock and TANGO2-depleted HepG2

cells in the control and nutrient-free medium. **H)** The fold change shows the ratio between reduced and oxidized lipid species in WT and TAN043 fibroblasts. A.U., means arbitrary units.

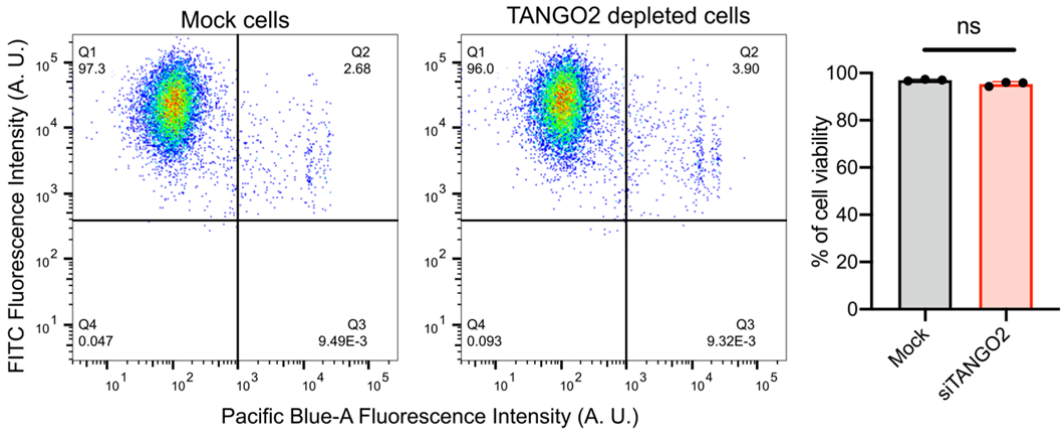

Figure 6 - Figure supplement 1. Cell viability of TANGO2-depleted cells. Mock and TANGO2-depleted cells were incubated with CellTrace Calcein Green AM (FITC) and DAPI (Pacific Blue-A) to determine cell viability by flow cytometry. Each dot in the dot plot graph represent one cell. Each dot in the column graph represent one of three independent experiments. A.U., means arbitrary units.

Discussion

TANGO2, a less studied protein from the TANGO collection, is gaining attention recently because of mutations in TANGO2 lead to severe pathologies (Bérat et al., 2021; Hoebeke et al., 2021; Miyake CY et al., 2022; Powell et al., 2021; Schymick et al., 2022; Yokoi et al., 2023). Patients with mutations in TANGO2 exhibit defects in cardiac and neuronal physiology leading to fatalities upon starvation and stress (https://tango2research.org) (Lalani et al., 2016; Miyake et al., 2022; Powell et al., 2021). Here we describe the physiological role of TANGO2 and its link to starvation-induced pathologies in patients.

TANGO2 functions in lipid homeostasis

TANGO2 has been shown to function at the mitochondria and in the ER-to-Golgi step of the protein secretion pathway (Bard et al., 2006; Milev et al., 2021). Our new data reveal that TANGO2 localizes predominantly to mitochondria, but also at sites on mitochondria that are juxtaposed to LDs, and ER (Figure 2 and S 1).

Loss of TANGO2 in HepG2 cells has revealed four clear features. 1, a change in the abundance of several phospholipids, mainly in the ratio of LPA to PA. LPA levels are elevated, and PA is reduced. 2, reduction in CL content. 3, increase in ROS and unsaturated lipid peroxidation levels. 4,

increase in LD size. The significance of these changes to TANGO2 function in physiology and pathology follows.

1. LPA is acylated to generate PA by lipid-modifying enzymes. The fact that LPA increases and PA decreases suggests that acylation of LPA is defective in TANGO2 lacking cells. The enzymes (LPAATs) involved in these acylation reactions are transmembrane proteins and acyl-CoA produced in the cytosol has to be imported into the lumen by membrane-embedded transporters (Gonzalez-Baro and Coleman, 2017; Lu and Claypool, 2015). TANGO2 lacks a transmembrane domain and cannot therefore function as an enzyme to catalyze these reactions in the lumen or the membrane of the ER or mitochondria. We suggest TANGO2 likely functions on the cytoplasmic face of mitochondria and the ER in the synthesis of acyl-CoA, or a carrier protein for acyl-CoA collection, or its metabolism. Our data show that although predominantly located to mitochondria, there is an enrichment of TANGO2 at sites juxtaposed to ER. This could be the site of LPA to PA conversion (Gonzalez-Baro and Coleman, 2017; Lu and Claypool, 2015). We suggest that without TANGO2, acyl-CoA is unavailable for the synthesis of PA from LPA. As a result, LPA levels rise with a concomitant drop in PA. This effect is exacerbated in nutrient-starved TANGO2-depleted cells. We noticed an increase in the

expression of GPAT and AGPAT in cells depleted of TANGO2. This suggests that cells sense a reduction in the levels of PA and upregulated these enzymes that convert G3P to LPA and LPA to PA Why don't we see restoration of PA levels in TANGO2-depleted cells. There are two possibilities; one, TANGO2 is necessary to collect acyl-CoA at the membrane and in its absence the cells do not have the pool of acyl-CoA available for producing PA. Two, in cells lacking TANGO2, there is an increase in ROS production, which modifies unsaturated fatty acids, which cannot be incorporated into PA. These possibilities remain untested.

2. A reduction in CL at the inner mitochondria membrane (Falabella et al., 2021; Paradies et al., 2019) is likely due to reduced LPA acylation because PA is a precursor to CL. Reduced CL in TANGO2-depleted cells could explain the consequent effects on mitochondria morphology and physiology (Heiman et al., 2022). In starving TANGO2-depleted cells, CL levels recover slightly compared to TANGO2-depleted cells. We suggest that when PA is low, cells likely use PG to produce CL (Falabella et al., 2021). This explains reduction in PG levels in starving TANGO2-depleted cells compared. Changes in CL are associated with a number of cardiac diseases (Dudek, 2017; Mulligan et al., 2014; Petrosillo et al., 2005). For example, Barth syndrome (BTHS) is an inherited

cardiomyopathy, associated with skeletal myopathy and growth retardation (Barth et al., 1996) , caused by a mutation in a mitochondria phospholipid-lysophospholipidtransacylase, involved in the biogenesis of CL (Dudek and Maack, 2017). These features are similar to the pathologies associated with TANGO2 mutations in humans.

3. Raising ROS levels cause mitochondria dysfunction (Bhatti et al., 2017; Sies and Jones, 2020). These oxidative modifications could alter the lipolytic mechanisms necessary to meet ATP demands during fasting. Moreover, high ROS levels cause peroxidation of unsaturated lipids that could be required in the LPA to PA step. Also, lipid peroxidation affects intracellular membranes, which could explain the effect of protein targeting and secretion (Sies and Jones, 2020).
4. Changes in LD volume are probably a reflection of increased incorporation to peroxidized lipids and a defect in catabolism. Several recent publications suggest that LD expansion upon oxidative stress is an evolutionarily conserved phenomenon to meliorated ROS-mediated lipid damage (Gasparian et al., 2022; Herms et al., 2013; Liu et al., 2015; Rambold et al., 2015). As a result, there is a defect in the availability of lipids for ATP production, mitochondria homeostasis, and cell signaling.

Altogether, TANGO2-depleted cells exhibit a change in lipid metabolism, which is aggravated in starving cells.

TANGO2 as a haem transfer protein

A paper published recently by Chen and colleagues showed that loss of human TANGO2 and its orthologs in yeast and worms caused accumulation of haem in compartments like the mitochondria and lysosome related organelles (LROs) (Sun et al., 2022). The authors showed that recombinant TANGO2 has low affinity binding to ferrous and ferric haem and adding recombinant TANGO2 to mitochondria enriched membrane fractions in vitro stimulated haem transfer to apo-myoglobin. They have concluded that haem is exported from the lumen into the cytoplasm by transmembrane transporters where it is captured by TANGO2 and subsequently transferred to specific clients. Surprisingly, this was observed even in trypsinized mitochondria and the authors concluded that cytoplasmic facing domains of transmembrane proteins or attached proteins are not required in TANGO2 mediated haem transfer. Why do TANGO2-depleted cells accumulate haem in mitochondria (or LROs)? If TANGO2 captures haem post its export from mitochondria, as is reported even in trypsinised mitochondria, then haem should be distributed into the cytoplasm and not retained in mitochondria or LROs. The data also do not correlate to the aggravated effects of TANGO2 depletion linked to human

pathologies, including a lack of any obvious sign of anaemia caused by defects in haem physiology. A plausible explanation for the reported data is that amphipathic haem is retained in mitochondria because of altered membrane lipid composition upon TANGO2 depletion. Further work is therefore required to clarify whether the proposed function of TANGO2 in haem transfer from mitochondria is an indirect consequence of dysfunctional mitochondria lipid composition.

Conclusion

We propose that TANGO2 has a function in events leading to specific-phospholipid production. Our data show a significant change in the ratio of LPA to PA in TANGO2-depleted cells. A defect in PA levels impacts the synthesis of mitochondria CL, and to balance this deficiency, the cells use other potential substrates, such as the PG, to produce CL. The net effect is an imbalance in lipid composition or homeostasis that, we suggest, also increases ROS levels and promotes lipid peroxidation. The acyl-CoA pathway is also used for the synthesis of numerous fatty acids, and a defect in its production would change the form and function of LDs to influence cellular lipid homeostasis. Sacher and colleagues have reconstituted many features of TANGO2 mutations in flies (Asadi et al., 2022). Interestingly, most of the aberrations in fly physiology are corrected, and an ER to Golgi transport defect in human cells by vitamin B5 supplement, which is used for the synthesis of CoA. In other words, loss of TANGO2 function is restored by replenishing or overdosing events leading to lipid neogenesis. CoA is used for acyl-CoA production, which is then used to acylate LPA to form PA. It has recently been shown that B-complex and multivitamins might prevent metabolic crises (Asadi et al., 2022; Miyake CY et al., 2022; Sandkuhler et al., 2022). However, why do multivitamins ameliorate metabolic crises in TANGO2 patients? Based on our results, we suggest that it is likely a combined effect of multivitamins on their antioxidant

627 properties and in stimulating new lipids biosynthesis. The starving cells
628 rely heavily on lipids for ATP production, and TANGO2-depleted are
629 therefore further stressed. Our findings thus reveal the physiological role of
630 TANGO2 and provide a handle to understand how its functional loss
631 triggers a variety of cardiac, muscular, and neurological pathologies
632 leading to fatalities upon conditions of starvation and stress.

Acknowledgements

We thank all members of the Malhotra laboratory for valuable discussions and critical reading of the manuscript. We thank Aida Rodriguez for advice with ROS analysis; Albert Pol and Albert Herms for advice with lipid metabolic experiments; the staff of the CRG/UPF Flow Cytometry Unit for advice with flow cytometry analysis and the staff of the CRG Advanced Light Microscopy Unit for invaluable technical help. We acknowledge the support of the Spanish Ministry of Science, the Centro de Excelencia Severo Ochoa, and the CERCA Programme / Generalitat de Catalunya. V. Malhotra is an Institució Catalana de Recerca i Estudis Avançats professor at the Centre for Genomic Regulation. V. Malhotra is an Institució Catalana de Recerca i Estudis Avançats professor at the Centre for Genomic Regulation Work in the Malhotra lab is funded by grants from the Spanish Ministry of Economy and Competitiveness (Plan Nacional to VM: PID2019-105518GB-I00) and the European Research Council Synergy Grant (ERC-2020-SyG-Proposal No. 951146). AL is funded by the European Molecular Biology Organization (EMBO ALTF 659-2021), JW is funded by the European Research Council (H2020-MSCA-IF-2019-894115). OF is funded by the Ramon y Cajal program (RYC-2016-20919). This work reflects only the authors' views, and the EU Community is not liable for any use that may be made of the information contained therein.

Materials and Methods

Cell culture

HepG2 cells (ATCC, Cat# HB-8065) were cultured in Dulbecco's Modified Eagle's Medium (DMEM; Lonza, Cat# SH30243.01) cell culture media supplemented with 10% (vol / vol) heat-inactivated fetal bovine serum (FBS; Gibco, Cat# 10270-106) (DMEM complete), 100 units/mL penicillin, and 100 µg/mL streptomycin (Gibco), at 37 °C in a humidified incubator supplied with 5% CO2. Primary dermal fibroblasts were isolated from healthy donors (WT) and TDD patients (exon 3-9 deletion mutation in TANGO2 gene; TAN043). Human skin fibroblasts were obtained with the patient's consent using the BCM IRB Protocol H-43240 (Baylor College of Medicine, Houston, TX, USA). Fibroblasts were cultured in DMEM medium supplemented with 20% (vol/vol) heat-inactivated FBS (FBS; Gibco, Cat# 10270-106), 100 units/mL penicillin, and 100 µg/mL streptomycin (Gibco) at 37 °C in a humidified incubator supplied with 5% CO2. For starvation conditions, cells were incubated in OptiMEM™ (Gibco, Cat# 11058021) without FBS for 4 h.

Plasmids, RNA interference, and cell transfection

For transient protein over-expression, cells were plated and 24 h later transfected with 1:1 ratio (DNA plasmid:Lipofectamine) using

Lipofectamine 3000 reagent (ThermoFisher Scientific) following manufacturer recommendations. Plasmids generated in our lab: TANGO2.Isoform1-EGFP, TANGO2.Isoform1-mScarlet, Peroxisome-SKL-mTurquoise2, GPAT4-Hairpin-mScarlet. Plasmids used and available from Addgene: ER-pmTurquoise2 (Addgene, Cat#36204), Mitochondria-pmTurquoise2 (Addgene, Cat#36208). For TANGO2 silencing, cells were plated and transfected with 1:3 ratio (RNA:Lipofectamine) using Lipofectamine RNAiMAX reagent (ThermoFisher Scientific) following manufacturer recommendations. 24 h after the first transfection, cells were transfected with a second and identical mix (ratio 1:3) of RNA:Lipofectamine. Two days after the second transfection, experiments described in this paper with siTANGO2 conditions were performed. TANGO2 RNAi sequences: Hs.Ri.TANGO2.13.1-SEQ1 (IDT technologies, Mfg ID# M498082302) and Hs.Ri.TANGO2.13.1-SEQ2 (IDT technologies, Mfg ID# M498082303).

Antibodies and Reagents

Primary antibodies used: anti-ADRP (Santa Cruz, Cat# sc-377429), anti-GFP (Roche, Cat# 11814460001), anti-β-actin (Sigma, Cat# A1978), anti-β-tubulin (Sigma, Cat# T4026), anti-Tom20 (Santa Cruz, Cat# sc-17764). Secondary antibodies used: Alexa Fluor 594 donkey anti-rabbit (Invitrogen, Cat# A21207), Alexa Fluor 594 donkey anti-mouse (Invitrogen, Cat#

A21203), Alexa Fluor 633 donkey anti-mouse (Invitrogen, Cat# A21050), Alexa Fluor 647 donkey anti-rabbit (Invitrogen, Cat# A31573), Alexa Fluor 647 donkey anti-mouse (Invitrogen, Cat# A31571), Alexa Fluor 680 donkey anti-rabbit (Invitrogen, Cat# A10043), Alexa Fluor 800 donkey anti-mouse (Invitrogen, Cat# A32789). Reagents used were: DAPI (Invitrogen, Cat# B223), Hoechst-33342 (Sigma, Cat# B2261), HCS LipidTOX™ Deep Red (ThermoFisher Scientific, Cat# H34477), Mitotracker™ Green (ThermoFisher Scientific, Cat# M7514), CellROX™ Deep Red (ThermoFisher Scientific, Cat# C10422), Image-iT™ Lipid Peroxidation Kit (ThermoFisher Scientific, Cat# C10445), CellTrace™ Calcein Green, AM (ThermoFisher Scientific, Cat# C34852), FluorSave™ reagent (Millipore, Cat# 345789-20), Lipofectamine™ RNAiMAX reagent (ThermoFisher Scientific, Cat# 13778075), Lipofectamine™ 3000 reagent (ThermoFisher Scientific, Cat# L3000015).

Immunoblotting

Immunoblot analysis was performed following the Biorad general protocol recommendations. Briefly, equal amounts of protein were resolved by SDS/PAGE, transferred onto 0.45-µm PVDF membranes (Amersham), and incubated overnight with anti-GFP (1:1000; Abcam), anti-β-actin (1:10,000; Sigma) antibodies followed by Alexa-conjugated secondary

antibodies (1:20,000; Invitrogen) for 1 h at 37 ºC. Bands were visualized an Odyssey CLX (LI-COR Biosciences).

Immunofluorescence and Immunohistochemistry

HepG2 cells (1×10^5 cells per well) were grown on coverslips. After mock or siTANGO2 silencing, cells were fixed with 3% paraformaldehyde, quenched, and incubated overnight with anti-ADRP (1:1000) at 4 ºC followed by Alexa Fluor 647 donkey anti-mouse (1:2000) and DAPI (1:10,000) for 1 h at 37 ºC. Coverslips were washed and mounted in FluorSave reagent. Samples were analyzed and high resolution images were acquired in an inverted Leica TCS SP8 confocal microscope equipped with photomultipliers and hybrid detectors. Images were processed using ImageJ software.

Forster Resonance Energy Transfer (FRET) measurement

For the energy donor and acceptor pair we selected NeonGreen and mScarlet respectively as they have been previously described as a suitable FRET pair (McCullock et al., 2020). To measure the energy transfer between the two we used the "acceptor photobleaching" method for its simplicity and robustness as has been previously described (Grecco and Bastiaens, 2013). By comparing the change in intensity of the quenched (pre photobleaching) and unquenched (post photobleaching) images of the

donor we can measure FRET between TANGO2.mScarlet and Tom20.Alexa633 using the following formula: FRET efficiency = 1 – (quenched donor / unquenched donor). To calculate the FRET efficiency we used averaged intensity values of each image. To calculate FRET maps we used pixel by pixel calculation of the FRET efficiency. All image calculations were processed using ImageJ software.

Live cell imaging

HepG2 cells (2.5×10^5 cells per dish) were grown on 35 mm polymer-bottom dishes (ibidi). After mock or siTANGO2 silencing, cells were washed and the cell medium was replaced with the appropriate conditioned medium for the indicated period of time. The cells were then washed several times to remove the conditioned medium and incubated with the appropriate reagent (Hoechst-33342, HCS LipiTOX Deep Red, MitoTracker Green). Finally, after several washes, cells were used to perform the experiments described in the paper. Samples were analyzed at 37 ºC in 5% CO2 atmosphere. High resolution and time-lapse images were acquired in an inverted Leica STELLARIS confocal microscope equipped with photomultipliers and hybrid detectors. Images were processed using ImageJ software. For co-localization analysis, we calculated the Pearson correlation coefficient (r) of confocal images with the coloc2 plugin in ImageJ software. To quantify the volume of LDs in confocal images, we

764 developed a macro to identify each voxel (pixel^3) stained by the lipophilic
765 marker LipidTOX in *z*-stacks. We then selected five *z*-stacks from each
766 condition. This macro automatically identified and distinguished the
767 positive from the negative particles on each slide and generated a data set
768 with the volume of each particle, the number of particles, and the total
769 volume of positive particles. This method reduced the chances in counting
770 errors or biases.
771
772 **Flow cytometry assays**
773 To examine the total LDs volume, HepG2 cells (2×10^5 cells per well)
774 were seeded in 24-well plates (ThermoFisher Scientific). Two days after
775 the second silencing (Mock or siTANGO2), cells were washed and the cell
776 medium was changed with the appropriate medium for the times indicated.
777 The cells were then washed several times to remove the conditioned
778 medium and incubated with the appropriate reagent (CellROX Deep Red,
779 Lipid Peroxidation Red/Green, HCS LipidTOX Deep Red, MitoTracker
780 Green, Calcein AM, DAPI). Cells were gently detached using trypsin and
781 washed several times before flow cytometry analyses. Flow cytometry
782 assays were performed by technical triplicates of at least 10,000 cells per
783 condition each time in three independent experiments. In the statistical
784 model these triplicates are nested together. Flow cytometry analysis was

performed using a BD LSR II Flow Cytometer (Becton Dickinson Biosciences).

Lipid extraction for mass spectrometry lipidomics

Mass spectrometry-based lipid analysis was performed by Lipotype GmbH (Dresden, Germany) as described (Surma et al., 2021). Lipids were extracted using a chloroform/methanol procedure (Ejsing CS et al., 2008). Samples were spiked with internal lipid standard mixture containing: cardiolipin 14:0/14:0/14:0/14:0 (CL), ceramide 18:1;2/17:0 (Cer), diacylglycerol 17:0/17:0 (DAG), hexosylceramide 18:1;2/12:0 (HexCer), lyso-phosphatidate 17:0 (LPA), lyso-phosphatidylcholine 12:0 (LPC), lyso-phosphatidylethanolamine 17:1 (LPE), lyso-phosphatidylglycerol 17:1 (LPG), lyso-phosphatidylinositol 17:1 (LPI), lyso-phosphatidylserine 17:1 (LPS), phosphatidate 17:0/17:0 (PA), phosphatidylcholine 17:0/17:0 (PC), phosphatidylethanolamine 17:0/17:0 (PE), phosphatidylglycerol 17:0/17:0 (PG), phosphatidylinositol 16:0/16:0 (PI), phosphatidylserine 17:0/17:0 (PS), cholesterol ester 20:0 (CE), sphingomyelin 18:1;2/12:0;0 (SM), triacylglycerol 17:0/17:0/17:0 (TAG). After extraction, the organic phase was transferred to an infusion plate and dried in a speed vacuum concentrator. The dry extract was re-suspended in 7.5 mM ammonium formiate in chloroform/methanol/propanol (1:2:4, V:V:V). All liquid handling steps were performed using Hamilton Robotics STARlet robotic

807 platform with the Anti Droplet Control feature for organic solvents
808 pipetting.
809
810 **MS data acquisition**
811 Samples were analyzed by direct infusion on a QExactive mass
812 spectrometer (Thermo Scientific) equipped with a TriVersa NanoMate ion
813 source (Advion Biosciences). Samples were analyzed in both positive and
814 negative ion modes with a resolution of Rm/z=200=280000 for MS and
815 Rm/z=200=17500 for MSMS experiments, in a single acquisition. MSMS
816 was triggered by an inclusion list encompassing corresponding MS mass
817 ranges scanned in 1 Da increments (Surma et al., 2015). Both MS and
818 MSMS data were combined to monitor CE, DAG and TAG ions as
819 ammonium adducts; LPC, LPC O-, PC, PC O-, as formiate adducts; and
820 CL, LPS, PA, PE, PE O-, PG, PI and PS as deprotonated anions. MS only
821 was used to monitor LPA, LPE, LPE O-, LPG and LPI as deprotonated
822 anions; Cer, HexCer and SM as formiate adducts.
823
824 **Lipidomics data analysis and post-processing**
825 Data were analyzed with an in-house developed lipid identification
826 software based on LipidXplorer (Herzog et al., 2012). Data post-processing
827 and normalization were performed using an in-house developed data
828 management system. Only lipid identifications with a signal-to-noise ratio

829 >5, and a signal intensity 5-fold higher than in corresponding blank
830 samples were considered for further data analysis.
831
832 **RNA extraction and Reverse Transcription Quantitative Polymerase**
833 **Chain Reaction (RT-qPCR)**
834
835 RNA was extracted using an RNeasy mini kit (QIAGEN, Hilden,
836 Germany) following manufacturer's instructions for direct cell lysis in a
837 12-well plate. Luna® Universal One-Step RT-qPCR Kit (New England
838 Biolabs, Ipswich, MA) was used for RT-qPCR reactions. Briefly, 10 µl
839 reaction contained: 5 µl Reaction MasterMix, 0.5 µl EnzymeMix, 0.8 µl
840 primers (10 µM, Fwd + Rv mixed), 1 µl of RNA (20 ng), 2.7 µl water. RT-
841 qPCR reactions were performed in duplicate or triplicate, and 3 biological
842 repeats were analyzed for each condition. RT-qPCRs were performed in a
843 LightCycler® 480 System (Roche, Basel, Switzerland) with conditions as
844 follows: 55°C for 10 minutes, 95°C for 1 minute, followed by 45 cycles of
845 95°C for 10 seconds, 60°C for 30 seconds. The cycle threshold value (Ct)
846 was calculated for each sample and normalized to GAPDH. The relative
847 expression levels were calculated using ΔΔCT method. Primer sequences
848 are included in the following table:

Gene	Forward primer (5' – 3')	Reverse primer (5' – 3')
AGPAT1	GGTACTCGCAACGACAATGG	TTGGTGTTGTAGAAGGAGGAGAAG

AGPAT2	AACGTGGCGCCTTCCA	GAAGTCTTGGTAGGAGGACATGACT
AGPAT3	CTCCAAGGTCCTCGCTAAGAAG	CCGCTTGCAGAACACAATCTC
AGPAT4	CACGGAATGCACCATCTTCA	GAACCACGATGGCATTTTCCT
AGPAT5	CTGGTGCTCCACACGTACTC	CCAGGCCAACACGTAGGTG
GPAT1	AACCCCAGTATCCCGTCTTT	CAGTCACATTGGTGGCAAAC
GPAT2	GGCTGACGGAGGAGATACTG	AGTTGTGCCAGGTGTGTGAG
GPAT3	ACAGCAGCCTCAAAAACTGG	CAATGGGGGAAGTATGGTTG
GPAT4	TGCCAAATGGGAGGTTTAAG	GCCACCATTTCTTGGTCTGT
LPIN1	CAGTCGAGGCTCAGACCA	TTCCCCGTTGATTTCTATGTCA
LPIN2	CCTCTCCTCAGACCAGATCG	GGAGAATCTGTCCCAAAGCA
LPIN3	AGAAGTCTTCACTGCAGCCC	CAGCTCCGAGTCGCTCTTAG
LPIN4	CCTTCAGCCTGACACAGAGG	AAGCGCTGCATTCTCAGAGT
PLA2G4A	TCTACAACCCCTGACAGCAG	GCTGTCCCTAGAGTTTCATCCA
TANGO2	CCGACCCTCCAAGTTAGCTG	TAGTTGGTGAGTGCTGCCAG
TANGO2	CACAGCAAAGGGAGACGTCA	GTTCCACAGCCTCCAGGAAG

Bioinformatic analysis

The repository used in the *In silico* analysis of TANGO2 orthologs and isoforms is available at https://github.com/alessiovignoli/TANGO2.

The code used in the development of the macro to identify each voxel (voxel = $pixel^3$ = pixel x pixel x pixel) is available at https://github.com/AAMateo/Lipid_Droplets.

Statistical analysis

Statistical analysis was performed using GraphPad Prism 8.0 (GraphPad) and R software. Data represent the mean ± SDs of N experiments. For simple unpaired analysis between two groups, Student's t-test with

subsequent Welch's correction was choosen. For multiple comparisons, ANOVA with subsequent Bonferroni's or Tukey's posttests was used. P values less than 0.05 were considered statistically significant.

References

Asadi P, Milev MP, Saint-Dic D, Gamberi C, Sacher M. 2022. Vitamin B5, a coenzyme A precursor, rescues TANGO2 deficiency disease-associated defects in Drosophila and human cells. *J Inherit Metab Dis*. doi:10.1002/jimd.12579

Bard F, Casano L, Mallabiabarrena A, Wallace E, Saito K, Kitayama H, Guizzunti G, Hu Y, Wendler F, DasGupta R, Perrimon N, Malhotra V. 2006. Functional genomics reveals genes involved in protein secretion and Golgi organization. *Nature* **439**:604–607. doi:10.1038/nature04377

Barth PG, Van Den Bogert C, Bolhuis PA, Scholte HR, Van Gennip ~ AH, Schutgens RBH, Ketel AG. 1996. X-Linked cardioskeletal myopathy and neutropenia (Barth syndrome): Respiratory-chain abnormalities in cultured fibroblasts, J. lnher. Metab. Dis.

Bérat CM, Montealegre S, Wiedemann A, Nuzum MLC, Blondel A, Debruge H, Cano A, Chabrol B, Hoebeke C, Polak M, Stoupa A, Feillet F, Torre S, Boddaert N, Bruel H, Barth M, Damaj L, Abi-Wardé MT, Afenjar A, Benoist JF, Madrange M, Caccavelli L, Renard P, Hubas A, Nusbaum P, Pontoizeau C, Gobin S, van Endert P, Ottolenghi C, Maltret A, de Lonlay P. 2021. Clinical and biological characterization of 20 patients with TANGO2 deficiency indicates novel triggers of metabolic crises and no primary energetic defect. *J Inherit Metab Dis* **44**:415–425. doi:10.1002/jimd.12314

Bhatti JS, Bhatti GK, Reddy PH. 2017. Mitochondrial dysfunction and oxidative stress in metabolic disorders — A step towards mitochondria based therapeutic strategies. *Biochim Biophys Acta Mol Basis Dis*. doi:10.1016/j.bbadis.2016.11.010

Broussard JA, Rappaz B, Webb DJ, Brown CM. 2013. Fluorescence resonance energy transfer microscopy as demonstrated by measuring the activation of the serine/threonine kinase Akt. *Nat Protoc* **8**:265–281. doi:10.1038/nprot.2012.147

Dudek J. 2017. Role of cardiolipin in mitochondrial signaling pathways. *Front Cell Dev Biol*. doi:10.3389/fcell.2017.00090

Dudek J, Maack C. 2017. Barth syndrome cardiomyopathy. *Cardiovasc Res*. doi:10.1093/cvr/cvx014

Ejsing CS, Sampaio JL, Surendranath V, Duchoslav E, Ekroos K, Klemm RW, Simons K, Shevchenko A. 2008. Global analysis of the yeast lipidome by quantitative shotgun mass spectrometry.

Falabella M, Vernon HJ, Hanna MG, Claypool SM, Pitceathly RDS. 2021. Cardiolipin, Mitochondria, and Neurological Disease. *Trends in Endocrinology and Metabolism*. doi:10.1016/j.tem.2021.01.006

Gasparian A, Aksenova M, Oliver D, Levina E, Doran R, Lucius M, Piroli G, Oleinik N, Ogretmen B, Mythreye K, Frizzell N, Broude E, Wyatt MD, Shtutman M. 2022. Depletion of COPI in cancer cells: the role of reactive oxygen species in the induction of lipid accumulation, noncanonical lipophagy and apoptosis. *Mol Biol Cell* **33**:ar135. doi:10.1091/mbc.E21-08-0420

Gonzalez-Baro MR, Coleman RA. 2017. Mitochondrial acyltransferases and glycerophospholipid metabolism. *Biochim Biophys Acta Mol Cell Biol Lipids* **1862**:49–55. doi:10.1016/j.bbalip.2016.06.023

Grecco HE, Bastiaens PIH. 2013. Quantifying cellular dynamics by fluorescence resonance energy transfer (FRET) microscopy. *Curr Protoc Neurosci*.

doi:10.1002/0471142301.ns0522s63
Heiman P, Mohsen AW, Karunanidhi A, St Croix C, Watkins S, Koppes E, Haas R, Vockley J, Ghaloul-Gonzalez L. 2022. Mitochondrial dysfunction associated with TANGO2 deficiency. *Sci Rep* **12**. doi:10.1038/s41598-022-07076-9
Herms A, Bosch M, Ariotti N, Reddy BJN, Fajardo A, Fernández-Vidal A, Alvarez-Guaita A, Fernández-Rojo MA, Rentero C, Tebar F, Enrich C, Geli MI, Parton RG, Gross SP, Pol A. 2013. Cell-to-cell heterogeneity in lipid droplets suggests a mechanism to reduce lipotoxicity. *Current Biology* **23**:1489–1496. doi:10.1016/j.cub.2013.06.032
Herzog R, Schuhmann K, Schwudke D, Sampaio JL, Bornstein SR, Schroeder M, Shevchenko A. 2012. Lipidxplorer: A software for consensual cross-platform lipidomics. *PLoS One* **7**. doi:10.1371/journal.pone.0029851
Hoebeke C, Cano A, De Lonlay P, Chabrol B. 2021. Clinical phenotype associated with TANGO2 gene mutation. *Archives de Pediatrie*. doi:10.1016/j.arcped.2020.11.004
Jennions E, Hedberg-Oldfors C, Berglund AK, Kollberg G, Törnhage CJ, Eklund EA, Oldfors A, Verloo P, Vanlander A V., De Meirleir L, Seneca S, Sterky FH, Darin N. 2019. TANGO2 deficiency as a cause of neurodevelopmental delay with indirect effects on mitochondrial energy metabolism. *J Inherit Metab Dis* **42**:898–908. doi:10.1002/jimd.12149
Kremer LS, Distelmaier F, Alhaddad B, Hempel M, Iuso A, Küpper C, Mühlhausen C, Kovacs-Nagy R, Satanovskij R, Graf E, Berutti R, Eckstein G, Durbin R, Sauer S, Hoffmann GF, Strom TM, Santer R, Meitinger T, Klopstock T, Prokisch H, Haack TB. 2016. Bi-allelic Truncating Mutations in TANGO2 Cause Infancy-Onset Recurrent Metabolic Crises with Encephalocardiomyopathy. *Am J Hum Genet* **98**:358–362. doi:10.1016/j.ajhg.2015.12.009
Lalani SR, Liu P, Rosenfeld JA, Watkin LB, Chiang T, Leduc MS, Zhu W, Ding Y, Pan S, Vetrini F, Miyake CY, Shinawi M, Gambin T, Eldomery MK, Akdemir ZHC, Emrick L, Wilnai Y, Schelley S, Koenig MK, Memon N, Farach LS, Coe BP, Azamian M, Hernandez P, Zapata G, Jhangiani SN, Muzny DM, Lotze T, Clark G, Wilfong A, Northrup H, Adesina A, Bacino CA, Scaglia F, Bonnen PE, Crosson J, Duis J, Maegawa GHB, Coman D, Inwood A, McGill J, Boerwinkle E, Graham B, Beaudet A, Eng CM, Hanchard NA, Xia F, Orange JS, Gibbs RA, Lupski JR, Yang Y. 2016. Recurrent Muscle Weakness with Rhabdomyolysis, Metabolic Crises, and Cardiac Arrhythmia Due to Bi-allelic TANGO2 Mutations. *Am J Hum Genet* **98**:347–357. doi:10.1016/j.ajhg.2015.12.008
Liu L, Zhang K, Sandoval H, Yamamoto S, Jaiswal M, Sanz E, Li Z, Hui J, Graham BH, Quintana A, Bellen HJ. 2015. Glial lipid droplets and ROS induced by mitochondrial defects promote neurodegeneration. *Cell* **160**:177–190. doi:10.1016/j.cell.2014.12.019
Lu YW, Claypool SM. 2015. Disorders of phospholipid metabolism: An emerging class of mitochondrial disease due to defects in nuclear genes. *Front Genet*. doi:10.3389/fgene.2015.00003
McCullock TW, MacLean DM, Kammermeier PJ. 2020. Comparing the performance of mScarlet-I, mRuby3, and mCherry as FRET acceptors for mNeonGreen. *PLoS One* **15**. doi:10.1371/journal.pone.0219886
Milev MP, Saint-Dic D, Zardoui K, Klopstock T, Law C, Distelmaier F, Sacher M. 2021. The phenotype associated with variants in TANGO2 may be explained by a dual role of the protein in ER-to-Golgi transport and at the mitochondria. *J Inherit*

Metab Dis **44**:426–437. doi:10.1002/jimd.12312
Mingirulli N, Pyle A, Hathazi D, Alston CL, Kohlschmidt N, O'Grady G, Waddell L, Evesson F, Cooper SBT, Turner C, Duff J, Topf A, Yubero D, Jou C, Nascimento A, Ortez C, García-Cazorla A, Gross C, O'Callaghan M, Santra S, Preece MA, Champion M, Korenev S, Chronopoulou E, Anirban M, Pierre G, McArthur D, Thompson K, Navas P, Ribes A, Tort F, Schlüter A, Pujol A, Montero R, Sarquella G, Lochmüller H, Jiménez-Mallebrera C, Taylor RW, Artuch R, Kirschner J, Grünert SC, Roos A, Horvath R. 2020. Clinical presentation and proteomic signature of patients with TANGO2 mutations. *J Inherit Metab Dis* **43**:297–308. doi:10.1002/jimd.12156
Miyake CY, Lay EJ, Beach CM, Ceresnak SR, Delauz CM, Howard TS, Janson CM, Jardine K, Kannankeril PJ, Kava M, Kim JJ, Liberman L, Macicek SL, Pham TD, Robertson T, Valdes SO, Webster G, Stephens SB, Milewicz DM, Azamian M, Ehsan SA, Houck KM, Soler-Alfonso C, Glinton KE, Tosur M, Li N, Xu W, Lalani SR, Zhang L. 2022. Cardiac crises: Cardiac arrhythmias and cardiomyopathy during TANGO2 deficiency related metabolic crises. *Heart Rhythm*. doi:10.1016/j.hrthm.2022.05.009
Miyake CY, Lay EJ, Soler-Alfonso C, Glinton KE, Houck KM, Tosur M, Moran NE, Stephens SB, Scaglia F, Howard TS, Kim JJ, Pham TD, Valdes SO, Li N, Murali CN, Zhang L, Kava M, Yim D, Beach C, Webster G, Liberman L, Janson CM, Kannankeril PJ, Baxter S, Singer-Berk M, Wood J, Mackenzie SJ, Sacher M, Ghaloul-Gonzalez L, Pedroza C, Morris SA, Ehsan SA, Azamian MS, Lalani SR. 2022. Natural history of TANGO2 deficiency disorder: Baseline assessment of 73 patients. *Genet Med*.
Mulligan CM, Le CH, Demooy AB, Nelson CB, Chicco AJ. 2014. Inhibition of delta-6 desaturase reverses cardiolipin remodeling and prevents contractile dysfunction in the aged mouse heart without altering mitochondrial respiratory function. *Journals of Gerontology - Series A Biological Sciences and Medical Sciences* **69**:799–809. doi:10.1093/gerona/glt209
Paradies G, Paradies V, Ruggiero FM, Petrosillo G. 2019. Role of cardiolipin in mitochondrial function and dynamics in health and disease: Molecular and pharmacological aspects. *Cells*. doi:10.3390/cells8070728
Petrosillo G, Di Venosa N, Ruggiero FM, Pistolese M, D'Agostino D, Tiravanti E, Fiore T, Paradies G. 2005. Mitochondrial dysfunction associated with cardiac ischemia/reperfusion can be attenuated by oxygen tension control. Role of oxygen-free radicals and cardiolipin. *Biochim Biophys Acta Bioenerg* **1710**:78–86. doi:10.1016/j.bbabio.2005.10.003
Powell AR, Ames EG, Knierbein EN, Hannibal MC, Mackenzie SJ. 2021. Symptom Prevalence and Genotype-Phenotype Correlations in Patients With TANGO2-Related Metabolic Encephalopathy and Arrhythmias (TRMEA). *Pediatr Neurol* **119**:34–39. doi:10.1016/j.pediatrneurol.2021.02.011
Rambold AS, Cohen S, Lippincott-Schwartz J. 2015. Fatty acid trafficking in starved cells: Regulation by lipid droplet lipolysis, autophagy, and mitochondrial fusion dynamics. *Dev Cell* **32**:678–692. doi:10.1016/j.devcel.2015.01.029
Raote I, Malhotra V. 2021. Annual Review of Biochemistry Tunnels for Protein Export from the Endoplasmic Reticulum. doi:10.1146/annurev-biochem-080120
Sandkuhler SE, Zhang L, Meisner JK, Ghaloul-Gonzalez L, Beach CM, Harris D, de Lonlay P, Lalani SR, Miyake CY, Mackenzie SJ. 2022. B-complex vitamins for patients with TANGO2-deficiency disorder. *J Inherit Metab Dis*. doi:10.1002/jimd.12585

Schymick J, Leahy P, Cowan T, Ruzhnikov MRZ, Gates R, Fernandez L, Pramanik G, Yarlagadda V, Wheeler M, Bernstein JA, Enns GM, Lee C, Acosta MT, Adam M, Adams DR, Agrawal PB, Alejandro ME, Alvey J, Amendola L, Andrews A, Ashley EA, Azamian MS, Bacino CA, Bademci G, Baker E, Balasubramanyam A, Baldridge D, Bale J, Bamshad M, Barbouth D, Bayrak-Toydemir P, Beck A, Beggs AH, Behrens E, Bejerano G, Bennet J, Berg-Rood B, Berry GT, Bican A, Bivona S, Blue E, Bohnsack J, Bonnenmann C, Bonner D, Botto L, Boyd B, Briere LC, Brokamp E, Brown G, Burke EA, Burrage LC, Butte MJ, Byers P, Byrd WE, Carey J, Carrasquillo O, Chang TCP, Chanprasert S, Chao HT, Clark GD, Coakley TR, Cobban LA, Cogan JD, Coggins M, Cole FS, Colley HA, Cooper CM, Cope H, Craigen WJ, Crouse AB, Cunningham M, D'Souza P, Dai H, Dasari S, Davis J, Dayal JG, Deardorff M, Dell'Angelica EC, Dhar SU, Dipple K, Doherty D, Dorrani N, Doss AL, Douine ED, Draper DD, Duncan L, Earl D, Eckstein DJ, Emrick LT, Eng CM, Esteves C, Falk M, Ferreira C, Fieg EL, Findley LC, Fisher PG, Fogel BL, Forghani I, Gahl WA, Glass I, Gochuico B, Godfrey RA, Golden-Grant K, Goldman AM, Goldrich MP, Goldstein DB, Grajewski A, Groden CA, Gutierrez I, Hahn S, Hamid R, Hanchard NA, Hantzaridis A, Hassey K, Hayes N, High F, Hing A, Hisama FM, Holm IA, Hom J, Horike-Pyne M, Huang A, Huang Y, Huryn L, Isasi R, Jamal F, Jarvik GP, Jarvik J, Jayadev S, Karaviti L, Kennedy J, Kiley D, Kobren SN, Kohane IS, Kohler JN, Krakow D, Krasnewich DM, Kravets E, Korrick S, Koziura M, Krier JB, Lalani SR, Lam B, Lam C, LaMoure GL, Lanpher BC, Lanza IR, Latham L, LeBlanc K, Lee BH, Lee H, Levitt R, Lewis RA, Lincoln SA, Liu P, Liu XZ, Longo N, Loo SK, Loscalzo J, Maas RL, MacDowall J, Macnamara EF, MacRae CA, Maduro V V., Mak BC, Malicdan MC V., Mamounas LA, Manolio TA, Mao R, Maravilla K, Markello TC, Marom R, Marth G, Martin BA, Martin MG, Martínez-Agosto JA, Marwaha S, McCauley J, McConkie-Rosell A, McCray AT, McGee E, Mefford H, Merritt JL, Might M, Mirzaa G, Morava E, Moretti PM, Mosbrook-Davis D, Mulvihill JJ, Murdock DR, Nagy A, Nakano-Okuno M, Nath A, Nelson SF, Newman JH, Nicholas SK, Nickerson D, Nieves-Rodriguez S, Novacic D, Oglesbee D, Orengo JP, Pace L, Pak S, Pallais JC, Palmer CGS, Papp JC, Parker NH, Phillips JA, Posey JE, Sacco L, Sampson JB, Samson SL, Saporta M, Scott CR, Schaechter J, Schedl T, Schoch K, Scott DA, Shashi V, Shin J, Signer R, Silverman EK, Sinsheimer JS, Sisco K, Smith EC, Smith KS, Solem E, Solnica-Krezel L, Solomon B, Spillmann RC, Stoler JM, Sullivan JA, Sullivan K, Sun A, Sutton S, Sweetser DA, Sybert V, Tabor HK, Tan ALM, Tan QKG, Tekin M, Telischi F, Thorson W, Thurm A, Tifft CJ, Toro C, Tran AA, Tucker BM, Urv TK, Vanderver A, Velinder M, Viskochil D, Vogel TP, Wahl CE, Wallace S, Walley NM, Walsh CA, Walker M, Wambach J, Wan J, Wang L kai, Wangler MF, Ward PA, Wegner D, Wener M, Wenger T, Perry KW, Westerfield M, Whitlock J, Wolfe LA, Woods JD, Yamamoto S, Yang J, Yousef M, Zastrow DB, Zein W, Zhao C, Zuchner S. 2022. Variable clinical severity in TANGO2 deficiency: Case series and literature review. *Am J Med Genet A* **188**:473–487. doi:10.1002/ajmg.a.62543

Sies H, Jones DP. 2020. Reactive oxygen species (ROS) as pleiotropic physiological signalling agents. *Nat Rev Mol Cell Biol*. doi:10.1038/s41580-020-0230-3

Sun F, Zhao Z, Willoughby MM, Shen S, Zhou Y, Shao Y, Kang J, Chen Y, Chen M, Yuan X, Hamza I, Reddi AR, Chen C. 2022. HRG-9 homologues regulate haem trafficking from haem-enriched compartments. *Nature* **610**:768–774. doi:10.1038/s41586-022-05347-z

Surma MA, Gerl MJ, Herzog R, Helppi J, Simons K, Klose C. 2021. Mouse lipidomics reveals inherent flexibility of a mammalian lipidome. *Sci Rep* **11**. doi:10.1038/s41598-021-98702-5

Surma MA, Herzog R, Vasilj A, Klose C, Christinat N, Morin-Rivron D, Simons K, Masoodi M, Sampaio JL. 2015. An automated shotgun lipidomics platform for high throughput, comprehensive, and quantitative analysis of blood plasma intact lipids. *European Journal of Lipid Science and Technology* **117**:1540–1549. doi:10.1002/ejlt.201500145

Tandon N, Thakkar K, LaGory E, Liu Y, Giaccia A. 2018. Generation of Stable Expression Mammalian Cell Lines Using Lentivirus. *Bio Protoc* **8**. doi:10.21769/bioprotoc.3073

Yokoi K, Nakajima Y, Takahashi Y, Hamajima T, Tajima G, Saito K, Miyai S, Inagaki H, Yoshikawa T, Kurahashi H, Ito T. 2023. Transport and Golgi organization 2 deficiency with a prominent elevation of C14:1 during a metabolic crisis: A case report. *JIMD Rep* **64**:3–9. doi:10.1002/jmd2.12275